Contemporary Mathematics
http://ojs.wiserpub.com/index.php/CM/

Research Article

Finite Difference and Machine Learning Simulation of Magneto-Tetra-Hybrid Nanofluid Transport in Time-Dependent Constricted Arteries

Muhammad Rooman[1], Nahid Fatima[2*], Zahir Shah[3*], Kamaleldin Abodayeh[2], Elisabeta Antonescu[4]

[1] Department of Mathematics, Gomal University, D.I. Khan 29050, Khyber Pakhtoonkhwa, Pakistan
[2] Department of Mathematics and Sciences, Prince Sultan University, Riyadh 11586, Saudi Arabia
[3] Department of Mathematical Sciences, University of Lakki Marwat, Lakki Marwat 28420, Khyber Pakhtunkhwa, Pakistan
[4] Faculty of Medicine, University Lucian Blaga of Sibiu, Sibiu 550024, Romania
E-mail: nfatima@psu.edu.sa (N.F.); Zahir@ulm.edu.pk (Z.S.)

Received: 20 February 2026; **Revised:** 16 April 2026; **Accepted:** 20 April 2026

Abstract: This research examines the unsteady Magnetohydrodynamic (MHD) tetra-hybrid nanofluid blood flow in a time-dependent stenosed artery, focusing on momentum transport, augmentation of heat transfer, enhancement of nanoparticle concentration, and entropy generation. By suspending four kinds of nanoparticles, namely copper Cu, aluminium oxide (Al_2O_3), titania (TiO_2) and gold (Au), the residence time is enhanced to form a Cu-Al_2O_3-TiO_2-Au/blood tetra-hybrid nanofluid in which blood acts as a non-Newtonian Jeffrey dendritic structure fluid. The issue is of great biomedical relevance, as highly stenosed arterial flow has a direct correlation with cardiovascular pathologies, while advanced nanofluid-based transport models can provide important insights for localized thermal control, drug delivery, and hemodynamic modulation in diseased vessels. The governing nonlinear dimensionless equations describing the velocity, temperature, concentration, and entropy characteristics are derived under suitably chosen physiological assumptions and solved numerically using an implicit Finite Difference Method (FDM). Furthermore, the Levenberg-Marquardt training algorithm-based Artificial Neural Network (ANN) model is applied for predicting the transport responses and examining the ability of data-driven approximation in comparison to numerical results. The numerical results are evident that the enhancement of the Jeffrey fluid parameter hastens the flow, and the volume/space effect of a stronger magnetic field hinders velocity subject to Lorentz forces with a rising temperature field. The ANN predictions agree well with the FDM solutions, demonstrating the robustness of the proposed hybrid computational framework. The novelty of the present work lies in the simultaneous evaluation of transient stenosed arterial transport under the MHD tetra-hybrid nanofluid model approach with a coupled FDM-ANN framework, advancing the prior studies by integrating unsteady arterial constriction effects, enhanced thermal transport characteristics, and entropy behavior as well as machine learning-enabled prediction in a consistent biomedical-oriented assessment. The current results could aid in the theoretical design of advanced hemodynamic and thermal management strategies across pathological arterial beds.

Keywords: stenosis, tetra-hybrid nanofluid, Jeffery fluid, viscous dissipation, Magnetohydrodynamic (MHD), Joule heating, entropy generation, Finite Difference Method (FDM), Artificial Neural Network (ANN)

MSC: 65N30, 68T07, 76Z05

Copyright ©2026 Muhammad Rooman, et al.
DOI: https://doi.org/10.37256/cm.7420269808
This is an open-access article distributed under a CC BY license
(Creative Commons Attribution 4.0 International License)
https://creativecommons.org/licenses/by/4.0/

Nomenclature

Symbol

b	Chemotaxis coefficient	
B_0	Magnetic field intensity	*tesla*
C	Nanoparticle concentration	
c_p	Specific heat	$\mathrm{J\,kg^{-1}\,K^{-1}}$
d	Distance of stenosis from origin	m
D_B	Brownian diffusion coefficient	$\mathrm{m^2\,s^{-1}}$
D_n	Microorganisms diffusion coefficient	$\mathrm{m^2\,s^{-1}}$
D_T	Diffusion coefficient	$\mathrm{m^2\,s^{-1}}$
E_0	externally applied electric field strength	$\mathrm{V\,m^{-1}}$
g	Gravitational acceleration	$\mathrm{9.8\,m\,s^{-2}}$
k	Thermal conductivity	$\mathrm{W\,m^{-1}\,K^{-1}}$
L	Length of artery	m
L_0	Length of stenosis	m
n	Density of motile microorganisms	$\mathrm{m^{-3}}$
p	Pressure	Pa
Q_0	Heat generation/absorption	
R	Radius of the artery (stenotic)	m
R_0	Radius of the artery (non-stenotic)	m
R_c	Chemical reaction	
W_c	Microorganism swimming speed	$\mathrm{m\,s^{-1}}$
t	Time	s
T	Temperature	K
$V(u,w)$	velocity	$\mathrm{m\,s^{-1}}$
(r,z)	Cylindrical coordinates	m

Greek letter

μ	Dynamic viscosity	$\mathrm{kg\,m^{-1}\,s^{-1}}$
ρ	Density	$\mathrm{kg\,m^{-3}}$
ρ_e	electric charge density	$\mathrm{C\,m^{-3}}$
σ	Electrical conductivity	$\mathrm{S\,m^{-1}}$
γ_T	Thermal expansion coefficient	
γ_C	Concentration expansion coefficient	
λ_1	relaxation to retardation time ratio	
λ_2	retardation time constant	
ϕ	Volume fraction	

Subscript

f	Base fluid
s_1	Cu nanoparticle
s_2	Al_2O_3 nanoparticle
s_3	TiO_2 nanoparticle

s_4	Au nanoparticle
nf	nanofluid
hnf	Hybrid nanofluid
$thnf$	Ternary-Hybrid nanofluid
$tethnf$	Tetra-Hybrid nanofluid
w	Wall

1. Introduction

The investigation of hemodynamics in stenosed arteries has a profound significance in the understanding of some cardiovascular diseases, which still rank among the top causes of deaths worldwide, such as angina pectoris, atherosclerosis, myocardial infarction, and aneurysms. Arterial stenosis is the constriction, or narrowing, of arteries; it is often associated with atherosclerosis. Atherosclerosis is a condition in which plaque buildup—made up of cholesterol, fat, calcium, and other substances clogs the inside walls of the arteries, interfering with normal blood flow. Such decreased blood flow grossly hampers the kidneys' capacity to filter waste, leading to a host of health problems, including high blood pressure. There are a large number of studies in the literature considering blood flow through stenosed arteries, specifically when nanomaterials are utilized to study these complex structures. Initial studies of stenosis concerned the effect of constriction in cylindrical ducts on flow investigated by Young [1], but subsequent work related stenoses to blood viscosity examined by Macdonald [2]. Recent work has also used computational fluid dynamics methods, including the finite volume method, to simulate blood flow in healthy arterial systems, which was investigated by Shareghi et al. [3]. Furthermore, Shahzadi and Bilal [4] examined studies considering stenosed arteries with application to drug delivery through these arteries.

The tetra-hybrid nanofluids are a relatively new area of research, revolutionizing conventional fluid mechanics by incorporating four species of nanoparticles into a single carrier fluid to acquire synergetic enhancement in the thermal as well as rheological characteristics, which can only be obtained using mono- or hybrid nanofluids. This advanced class of nanofluids possesses unprecedented tunability of important thermophysical characteristics, including thermal conductivity, viscosity, electrical conductivity, and entropy generation—these attributes are crucial for emerging biomedical applications in targeted drug delivery, hyperthermia-based cancer therapy, and magnetically controlled hemodynamic management. Recently, Singh and Nandkeolyar [5] examined the flow of a tetra-hybrid nanofluid model past a stenosed artery modeled by Casson fluid in a non-Darcy porous medium as well as utilized the spectral quasi-linearization method along with an Artificial Neural Network (ANN). They showed that temperature increases with radiation, magnetic, Eckert, and porosity parameters, but its reverse form is for velocity. Sudarmozhi et al. [6] recently performed an extensive study on the effect of Soret-Dufour on Williamson fluid flow with tetra-hybrid nanoparticles (Au, Ag, TiO_2, Al_2O_3) under Magnetohydrodynamic (MHD), porous medium, radiative flux, and Joule heating, where they applied ANN for prediction about outcomes and reported that Soret-Dufour effects have a very significant enhancement in Nusselt number as well as Sherwood number. Singh et al. [7] investigated the transport of tetra-hybrid nanofluid for shrinking and stretching needles with gyrotactic microorganisms, activation energy, and slip conditions using the finite element method; it was found that the Nusselt number, Sherwood number, and shear stress numbers are enhanced with increasing size of the needle. Hafed et al. [8] studied tetra-hybrid nanofluids of oxytactic microorganisms under forced blood flow in a stenosed artery and reported that the highest heat transport was provided by tetra-hybrids compared to mono-, di-, and trihybrid configurations.

In the context of biomedical engineering, MHD offers enormous potential for drug delivery, wound healing, controlling blood loss during surgery, and enhancing the functionality of medical instruments (drug carriers, magnetic tracers, and blood pumps, among others). The electrically conductive nature of blood allows for the possibility that MHD principles could be applied. It's worth noting that Alghamdi et al. [9] and Saeed et al. [10] have considered MHD hybrid nanofluid flow in a blood vessel to investigate the influence of the electromagnetic field and couple stresses on blood flow. Nadeem et al. [11] and Majee and Shit [12] also studied the impact of MHD on the blood flow in stenosed arteries and found

that strong static transverse magnetic fields can decrease blood flow velocity in stenotic regions, leading to an increase in childhood risk factors for downstream plaque formation.

Entropy, which is a prime concept of thermodynamics, leads us to understand how energy conversion in fluid systems will be applied inefficiently. In human blood flow through stenotic arteries, the utilization of entropy is crucial to minimize loss and enhance efficiency. Studies by Sharma et al. [13], Gandhi et al. [14], and others have studied entropy generation in blood flowing with viscous dissipation, radiation effects, chemical reaction, and Joule heating. These works have used hybrid particles to maximize entropy on curved and stenosed arteries and thus the possibility of new approaches for promoting blood flow hemodynamics [15].

Most existing research is based on the Newtonian fluid assumption; however, recent studies have acknowledged the need to represent blood as a non-Newtonian fluid, especially in smaller vessels and in capillaries. The Jeffrey fluid, a commonly cited model for studying blood viscoelasticity, offers a balance between computational ease and complexity. Studies such as [16, 17] and Padma et al. [18] have considered blood flow in stenosed arteries with nanoparticles by the Jeffrey model, considered slip effects and magnetic field effects. Kumar et al. [19] conducted a sensitivity study of the Jeffrey nanofluid flow using copper nanoparticles and polyvinyl alcohol water as the base fluid. Using the Jeffrey fluid model for blood behavior characterization, Ali et al. [20] did simulations to examine the peristaltic transmission of hybrid nano-blood assisted by cilia through an arterial tube.

Researchers are now adopting AI-based computational solvers to address challenging open problems in a wide spectrum of applied science endeavors. Within these methods, ANNs have been increasingly used, especially in the context of fluid mechanics, due to their ability to learn complex input–output relationships and efficiently represent solutions. Outside the field of fluid mechanics, ANN-based models are also frequently adopted in aeronautics, automotive engineering and weather forecasting for flow or evolving fluid-pattern dynamics prediction. Scientists have also used ANN algorithms to investigate complex systems of nuclear physics, non-linear electric circuits, astrophysics, thermodynamics and MHD. These ANN techniques usually involve learning from datasets instead of deriving them in the traditional manner. Therefore, a great many scholars have used ANNs to predict heat transfer and fluid flow. For instance, Çolak et al. [21] presented an ANN model and analyzed reliability with a Rayleigh distribution as well as an inverse power-law structure. Shafiq et al. [22] used ANNs to study tangent-hyperbolic Darcy-Forchheimer flow over a cylinder, considering the rheological characteristics of Newtonian and tangent-hyperbolic fluids to more accurately represent the physical response. Qureshi et al. [23] used ANN models to accurately predict the heat transfer behavior of Hybrid Nanofluid (HNFs). In another study, Ermiş et al. [24] used ANNs to investigate the heat transfer mechanism in finned-tube Latent Heat Thermal Energy Storage (LHTES) with emphasis on phase change phenomena. A recent study [25] introduced a novel framework for modeling blood flow and heat transfer in non-planar curved arteries, highlighting the potential of machine-learning-assisted simulations for biomedical flow analysis. Recently, Rehman et al. [26] utilized artificial neural network engineering using the Levenberg-Marquardt algorithm to suggest the Nusselt number of a uniformly heated Y-shaped fin in an incompletely heated hexagonal cavity subjected to normal convection and magnetic field effects. The study showed the potential of ANN to mimic complex heat transfer behavior in Casson fluid profiles under heated and cold fin tip conditions, representing a data-driven alternative to traditional simulations. Kousar et al. [27] proposed an artificial neural network model with three inputs, ten hidden layers, and one output that was trained using the Levenberg-Marquardt algorithm to predict kinetic energy values of Casson fluid in a staggered cavity under a natural convection flow and inclined magnetic field. Rehman et al. [28] utilized a neural artificial intelligence to predict the mass transfer coefficient in Carreau fluid flow over a magnetized porous flat surface with velocity and temperature slip, where the proposed neural model employed a single hidden layer of ten neurons that were trained through the Levenberg-Marquardt method.

While the application of tetra-hybrid nanofluids to blood is still significantly theoretical at this stage, these recent advancements in nanomedicine and targeted drug delivery systems highlight that multifunctional nanoparticles can be engineered for biomedical-related applications. Hybrid and multi-component nanoparticles have been investigated to improve thermal transport and imaging and enable controlled drug release. Thus, the current model should be interpreted as a forward-looking framework that gives theoretical insight into the potential behavior of such advanced nanofluid systems under pathological conditions, especially on stenosed conduits.

Motivated by the above facts, the purpose of this paper is to conduct a detailed numerical and data-driven study on unsteady mixed convection flow, heat and mass transfer, and bioconvective microorganism transport in tetra-hybrid nanofluid under MHD effects, thermal radiation, and non-Newtonian behavior. The connected nonlinear equations that govern the model are solved with a stable implicit finite difference scheme, which relies on the Thomas algorithm and includes strong multiphysics problems. Besides the transport study, a comprehensive heat transfer analysis is also performed based on entropy generation and the Bejan number in order to quantify sources of irreversibility due to heat transfer, viscous dissipation, and Joule heating. In addition, an ANN methodology is established as a fast and accurate surrogate utilizing a numerically generated database for the prediction of velocity, temperature, nanoparticle concentration, microorganism concentration, and entropy-related parameters over wide-ranging controlling parameters. The ordering mechanism of the reportable results represents a computationally effective manner of predicting the mixed convective bioconvection to be further exploited for practical purposes in biomedical engineering, thermal control, and advanced energy conversion systems. The main novelty of the current work lies in the simultaneous integration of the modeling of unsteady stenosed arterial flow under MHD and coupled analysis of momentum, thermal, concentration, and entropy generation using an FDM-ANN predictive framework for tetra-hybrid nanofluid transport within a single biomedical modeling context. To the authors' best knowledge, earlier studies have generally examined these aspects in a partial or isolated manner, while the current study presents all three elements in a unified model and shows that they act as coupled factors influencing pathological arterial transport. This allows it to extend the prior literature with both improved physical modeling and data-driven prediction of complex hemodynamic systems.

2. Problem description and mathematical formulation

The physical model considers the unsteady, axisymmetric flow of a blood-based tetra-hybrid nanofluid through an idealized stenosed artery of finite length. For instance, the arterial segment is represented as a rigid cylindrical tube, where symmetric stenosis of finite length is produced within a certain axial section. As depicted in Figure 1a, a cylindrical coordinate system $(r,\ z)$ is utilized, where z describes the axial direction along the artery and r corresponds to the radial coordinate from the centerline. The mechanical properties of stenosis geometry are defined by its axial location, length, and maximum (severity) height. These three parameters define the level of lumen constriction. The inlet corresponds to the upstream healthy arterial segment, and the outlet refers to the downstream recovery region. The centerline meets the symmetry condition, and the arterial wall is presupposed to be rigid and impermeable. The stenosis geometry is represented using a time-dependent mathematical expression, the defining parameters (severity, length, and location) of which are explicitly controlled. Stenosis severity and length are chosen according to [29] to maintain consistency with other models in literature. The currently considered idealized arrangement is used to focus on the dominant effects of stenosis and tetra-hybrid nanofluid transport in a computationally feasible manner. The tetra-hybrid blood-based nanofluid is illustrated in Figure 1b.

The mathematical model of the non-Newtonian, time-dependent multi-stenosis is defined by the geometry given in Ahmed and Nadeem [29]:

$$R(z)=\begin{cases}\left[R_0-\frac{2\delta^*}{L_0}(z-2d)\right]\Omega(t), & d\le z\le d+L_0/2\\ \left[R_0+\frac{\delta^*}{5}\left(\frac{4}{5}L_0-\frac{11}{5}d\right)\right]\Omega(t), & d+L_0/2\le z\le d+3L_0/2\\ \left[R_0+2\frac{\delta^*}{L_0}(z-d-L_0)\right]\Omega(t), & d+3L_0/2\le z\le d+2L_0\\ \left[R_0+\frac{\delta^*}{L_0}\sin(\pi(z-d))\right]\Omega(t), & d+2L_0\le z\le d+3L_0\\ R_0\Omega(t), & \text{otherwise}.\end{cases} \tag{1}$$

The parameter that varies throughout time is provided by [29]:

$$\Omega(t) = 1 - \lambda\,(\cos \omega t - 1)\, e^{-\lambda \omega t}. \tag{2}$$

In this study, the axisymmetric flow is considered and no azimuthal coordinate (θ) is taken into account. In equation (1), R_0 represent the radius of non-diseased arteries, while $R(z)$ signifies the stenosis radius. In this context, the symbol δ^* refers to the height of the stenosis, d denotes the distance from the origin to a zone where stenosis occurs, and L_0 represents the maximum length of the stenotic sections. The model relies on the following assumptions:

• The flow is pulsatile, incompressible, and bidirectional for the stenosed cylindrical artery.

• The flow exhibits axisymmetry.

• The fields of velocity, temperature, concentration, and microorganism distribution of the nanoparticles are formulated as:

$$\left.\begin{aligned} \overrightarrow{V} &= (u(r,\, z,\, t),\, 0,\, w(r,\, z,\, t)) \\ T &= T(r,\, z,\, t) \\ C &= C(r,\, z,\, t) \\ n &= n(r,\, z,\, t) \end{aligned}\right\} \tag{3}$$

In Eq. (3), u and w are radial and axial velocities, respectively.

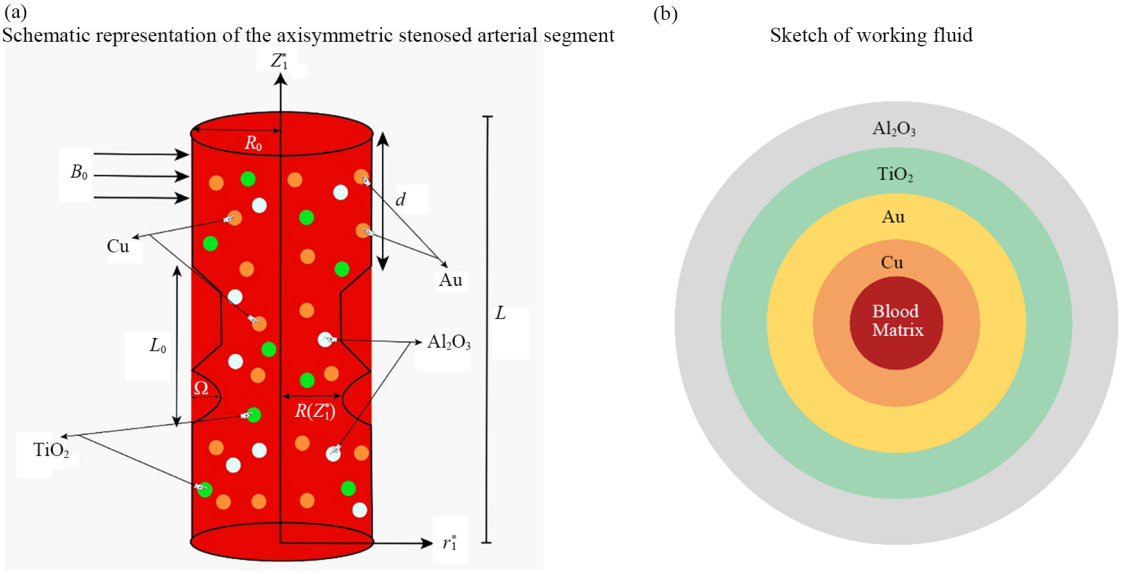


Figure 1. Schematic representation of the axisymmetric stenosed arterial segment and working fluid

2.1 *Governing equations*

Using the Jeffrey fluid model [16, 30, 31], we obtain the following governing equations for mass, momentum, and energy conservation, as well as nanoparticle concentration:

The stated continuity equation is used to enforce conservation of mass and, thus, characterizes the incompressible nature of blood-based tetra-hybrid nanofluid in the stenosed duct portion.

$$\frac{\partial \overline{u}}{\partial \overline{r}} + \frac{\overline{u}}{\overline{r}} + \frac{\partial \overline{w}}{\partial \overline{z}} = 0. \tag{4}$$

The momentum equation includes a balance between the applied pressure gradient and opposing supporting transport mechanisms in the stenotic artery.

$$\rho_{tethnf}\left[\frac{\partial \overline{u}}{\partial \overline{t}} + \overline{u}\frac{\partial \overline{u}}{\partial \overline{r}} + \overline{w}\frac{\partial \overline{u}}{\partial \overline{z}}\right] = -\frac{\partial \overline{p}}{\partial \overline{r}} + \frac{1}{\overline{r}}\frac{\partial}{\partial \overline{r}}\left(\overline{r}\tau_{\overline{r}\overline{r}}\right) + \frac{\partial}{\partial \overline{z}}\left(\tau_{\overline{z}\overline{r}}\right), \tag{5}$$

$$\begin{aligned}\rho_{tethnf}\left[\frac{\partial \overline{w}}{\partial \overline{t}} + \overline{u}\frac{\partial \overline{w}}{\partial \overline{r}} + \overline{w}\frac{\partial \overline{w}}{\partial \overline{z}}\right] &= -\frac{\partial \overline{p}}{\partial \overline{z}} + \frac{1}{\overline{r}}\frac{\partial}{\partial \overline{r}}\left(\overline{r}\tau_{\overline{r}\overline{z}}\right) + \frac{\partial}{\partial \overline{z}}\left(\tau_{\overline{z}\overline{z}}\right) + \rho_e E_0 + G\left(\overline{t}\right) \\ &\quad + \left(\rho\gamma_T\right)_{tethnf} g\left(T - T_1\right) + \left(\rho\gamma_C\right)_{tethnf} g\left(C - C_1\right) - \sigma_{tethnf} B_0^2 \overline{w}.\end{aligned} \tag{6}$$

Eq. (5) describes the momentum balance in the radial direction, while Eq. (6) defines the axial momentum balance. In both equations, unsteady acceleration and convective inertia terms appear on the left-hand side and pressure gradients along with other viscous terms on the right-hand side. The thermal and solutal buoyancy forces are included in the axial momentum equation, together with the externally applied electric field $(\rho_e E_0)$, the time-dependent driving force $G(\overline{t})$, and the magnetic Lorentz force $(\sigma_{tethnf} B_0^2 \overline{w})$, which serves as a resistive body force that inhibits the axial movement of fluid.

The equation for thermal energy can be written in the following form:

$$\begin{aligned}\left(\rho C_P\right)_{tethnf}\left[\frac{\partial T}{\partial \overline{t}} + \overline{u}\frac{\partial T}{\partial \overline{r}} + \overline{w}\frac{\partial T}{\partial \overline{z}}\right] &= k_{tethnf}\left[\frac{\partial^2 T}{\partial \overline{r}^2} + \frac{1}{\overline{r}}\frac{\partial T}{\partial \overline{r}} + \frac{\partial^2 T}{\partial \overline{z}^2}\right] + Q_0 + \sigma_{tethnf} B_0^2 \overline{w}^2 \\ &\quad + \left(\rho C_P\right)_{tethnf}\left[D_B\left(\frac{\partial C}{\partial \overline{r}}\frac{\partial T}{\partial \overline{r}} + \frac{\partial C}{\partial \overline{z}}\frac{\partial T}{\partial \overline{z}}\right)\right. \\ &\quad \left. + \frac{D_T}{\left(T_w - T_1\right)}\left(\left(\frac{\partial T}{\partial \overline{r}}\right)^2 + \left(\frac{\partial T}{\partial \overline{z}}\right)^2\right)\right] + \sigma_{tethnf} E_0^2 + \phi^*,\end{aligned} \tag{7}$$

where ϕ^* is defined as:

$$\phi^* = 2\mu_{tethnf}\left(\frac{1}{1+\lambda_1}\right)\left[\left(\frac{\partial \overline{u}}{\partial \overline{r}}\right)^2 + \left(\frac{\overline{u}}{\overline{r}}\right)^2 + \left(\frac{\partial \overline{w}}{\partial \overline{z}}\right)^2 + \frac{1}{2}\left(\frac{\partial \overline{u}}{\partial \overline{z}} + \frac{\partial \overline{w}}{\partial \overline{r}}\right)^2\right].$$

The transport of thermal energy in blood-based tetra-hybrid nanofluid is described by Eq. (7). The left-hand side indicates the transient and convective heat transport, whereas the right-hand side demonstrates thermal conduction, internal heat generation/absorption (Q_0), magnetic Joule heating $(\sigma_{tethnf} B_0^2 \overline{w}^2)$, and electric Joule heating $(\sigma_{tethnf} E_0^2)$ as well as Brownian motion-induced thermal transport, thermophoretic heat transport, and viscous dissipation represented through term ϕ^*. These collectively represent the dominating thermal modes that affect the temperature field in the stenosed arterial flow.

The nanoparticle concentration is described by the equation:

$$\frac{\partial C}{\partial \bar{t}}+u\frac{\partial C}{\partial \bar{r}}+\overline{w}\frac{\partial C}{\partial \bar{z}}=D_B\left[\frac{\partial^2 C}{\partial \bar{r}^2}+\frac{1}{\bar{r}}\frac{\partial C}{\partial \bar{r}}+\frac{\partial^2 C}{\partial \bar{z}^2}\right]+\frac{D_T}{(T_w-T_1)}\left[\frac{\partial^2 T}{\partial \bar{r}^2}+\frac{1}{\bar{r}}\frac{\partial T}{\partial \bar{r}}+\frac{\partial^2 T}{\partial \bar{z}^2}\right]-R_c\,(C-C_1)\,, \tag{8}$$

that accounts for the combined influence of unsteady transport, convection, Brownian diffusion, thermophoretic diffusion, and first-order chemical reaction on the nanoparticle concentration distribution. The term associated with D_B represents the Brownian motion of nanoparticles, while the term governing D_T indicates thermophoretic migration due to temperature gradients. The term representing the change due to reaction: $R_c(C-C_1)$ describes the consumption or generation of species via chemical reaction.

For the inclusion of bioconvective effects, we have the conservation equation for the density of motile microorganisms n expressed as:

$$\frac{\partial n}{\partial \bar{t}}+\overline{u}\frac{\partial n}{\partial \bar{r}}+\overline{w}\frac{\partial n}{\partial \bar{z}}+\frac{bW_c}{C_0-C_w}\left[\frac{\partial}{\partial \bar{r}}\left(n\frac{\partial C}{\partial \bar{r}}\right)+\frac{\partial}{\partial \bar{z}}\left(n\frac{\partial C}{\partial \bar{z}}\right)\right]=D_n\left[\frac{\partial^2 n}{\partial \bar{r}^2}+\frac{1}{\bar{r}}\frac{\partial n}{\partial \bar{r}}+\frac{\partial^2 n}{\partial^2 \bar{z}}\right]. \tag{9}$$

Microbial motility coordination within the flow domain is represented by Equation (9). It considers unsteady transport (due to both fluid convective and microorganism diffusion), including bioconvective migration induced by concentration gradients. The additional transport term $bW_c/(C_0-C_w)$ describes the directed movement of microorganisms due to local fluctuations in nanoparticle concentration that plays a role in bioconvective stability of suspension.

The non-zero components of the Jeffrey fluid extra stress tensor $\tau_{\overline{rr}}$, $\tau_{\overline{rz}}$ and $\tau_{\overline{zz}}$ in equations (5) and (6) are given below [16]:

$$\left.\begin{aligned}
\tau_{\overline{rr}} &= \tfrac{2\mu_{tethnf}}{1+\lambda_1}\left[1+\lambda_2\left(\overline{u}\tfrac{\partial}{\partial \bar{r}}+\overline{w}\tfrac{\partial}{\partial \bar{z}}\right)\right]\tfrac{\partial \overline{u}}{\partial \bar{r}},\\
\tau_{\overline{rz}} &= \tfrac{\mu_{tethnf}}{1+\lambda_1}\left[1+\lambda_2\left(\overline{u}\tfrac{\partial}{\partial \bar{r}}+\overline{w}\tfrac{\partial}{\partial \bar{z}}\right)\right]\left(\tfrac{\partial \overline{u}}{\partial \bar{z}}+\tfrac{\partial \overline{w}}{\partial \bar{r}}\right),\\
\tau_{\overline{zz}} &= \tfrac{2\mu_{tethnf}}{1+\lambda_1}\left[1+\lambda_2\left(\overline{u}\tfrac{\partial}{\partial \bar{r}}+\overline{w}\tfrac{\partial}{\partial \bar{z}}\right)\right]\tfrac{\partial \overline{w}}{\partial \bar{z}}.
\end{aligned}\right\} \tag{10}$$

These constitutive relations describe the non-Newtonian rheology of a Jeffrey fluid, with λ_1 and λ_2 being the relaxation to retardation time ratio and the retardation time constant, respectively. The first parameter λ_1 governs the elastic memory effect of the aforementioned fluid, while λ_2 reflects the retardation behavior via deformation history.

In equation (6), G(t$\overline{\ }$) reflects the body's axial acceleration as provided by [32]:

$$G(\bar{t})=a_0\cos(w_b\bar{t}+\phi_b),\ \bar{t}>0\,,$$

$$\phi_b=2\pi f_b,$$

where ϕ_b, a_0, and f_b are the phase angle, body acceleration amplitude, and frequency.

The boundary conditions are as follows [33]:

$$\overline{w}=w_B,\ T=T_w,\ C=C_w,\ n=n_w \qquad \text{at} \quad \bar{r}=R(\bar{z}), \tag{11}$$

$$\frac{\partial \overline{w}}{\partial \overline{r}} = 0, \ \frac{\partial T}{\partial \overline{r}} = 0, \ \frac{\partial C}{\partial \overline{r}} = 0, \ \frac{\partial n}{\partial \overline{r}} = 0 \quad \text{at} \quad \overline{r} = 0. \tag{12}$$

The initial conditions are [33]:

$$\overline{w} = 0, \ T = 0, \ C = 0, \ n = 0 \quad \text{at} \quad \overline{t} = 0, \tag{13}$$

Electro-osmosis equation is as follows [34]:

$$\left(\frac{\partial^2}{\partial \overline{r}^2} + \frac{1}{\overline{r}} \frac{\partial}{\partial \overline{r}} + \frac{\partial^2}{\partial \overline{z}^2} \right) \Phi = \frac{\Phi}{q_m^2}, \tag{14}$$

where $q_m = \frac{1}{e_0 z_0} \sqrt{\frac{\varepsilon k_B T_{\text{avg}}}{2 s_0}}$.

The subsequent boundary conditions pertain to the electro-osmotic equation [34]:

$$\begin{cases} \Phi = 0.3\zeta & \text{at} \quad \overline{r} = R(\overline{z}), \\ \dfrac{\partial \Phi}{\partial \overline{r}} = 0 & \text{at} \quad \overline{r} = 0, \\ \Phi = 0.1\zeta & \text{at} \quad \overline{r} = R(\overline{z}). \end{cases} \tag{15}$$

2.2 *Dimensionless variables and parameters*

The suggested model can be rendered dimensionless by employing the subsequent scaling factors shown in Table 1; Table 2 demonstrates the range of dimensionless key parameters.

Table 1. Dimensionless parameters and their physical meaning

Symbol	Parameter	Physical meaning
$r = \frac{\overline{r}}{R_0}$	Radial coordinate	Non-dimensional radial distance
$z = \frac{\overline{z}}{l_0}$	Axial coordinate	Non-dimensional axial distance
$t = \frac{U_0 \overline{t}}{R_0}$	Time	Non-dimensional time variable
$w = \frac{\overline{w}}{U_0}$	Axial velocity	Dimensionless axial velocity
$u = \frac{l_0 \overline{u}}{\delta^* U_0}$	Radial velocity	Dimensionless radial velocity
$R = \frac{\overline{R}}{R_0}$	Artery radius	Dimensionless arterial radius
$p = \frac{R_0^2 \overline{p}}{U_0 l_0 \mu_f}$	Pressure	Dimensionless pressure
$\theta = \frac{T - T_1}{T_w - T_1}$	Temperature	Dimensionless temperature
$\sigma = \frac{C - C_1}{C_w - C_1}$	Concentration	Dimensionless nanoparticle concentration
$\chi = \frac{n - n_1}{n_w - n_1}$	Microorganism density	Dimensionless microorganism concentration
$E = \frac{E_0}{B_0 U_0}$	Electric field	Dimensionless electric field
$Re = \frac{\rho_f U_0 R_0}{\mu_f}$	Reynolds number	Ratio of inertial to viscous forces
$Pr = \frac{(C_P)_f \mu_f}{k_f}$	Prandtl number	Ratio of momentum to thermal diffusivity
$Ec = \frac{U_0^2}{C_p (T_w - T_1)}$	Eckert number	Measures viscous dissipation
$Br = RePr = \frac{\mu_f U_0^2}{k_f (T_w - T_1)}$	Brinkman number	Ratio of viscous dissipation to heat conduction

Table 1. (cont.)

Symbol	Parameter	Physical meaning
$M = \frac{\sigma_f}{\mu_f} B_0^2 R_0^2$	Magnetic parameter	Measures Lorentz force effect
$Gr_T = \frac{\rho_f g R_0^2 \gamma_T (T_w - T_1)}{\mu_f U_0}$	Thermal Grashof number	Buoyancy due to temperature
$Gr_C = \frac{\rho_f g R_0^2 \gamma_C (C_w - C_1)}{\mu_f U_0}$	Solutal Grashof number	Buoyancy due to concentration
$N_b = \frac{\rho_f (C_P)_f D_B C_1}{k_f}$	Brownian motion parameter	Effect of Brownian diffusion
$N_t = \frac{\rho_f D_T (C_p)_f}{k_f}$	Thermophoresis parameter	Effect of thermophoretic diffusion
$Le = \frac{\mu_f}{\rho_f D_B}$	Lewis number	Ratio of thermal to mass diffusivity
$Sc = \frac{\nu}{D_m}$	Schmidt number	Ratio of momentum to mass diffusivity
$Pe = \frac{bW_c}{D_{n_2}}$	Peclet number	Ratio of convection to diffusion
$Q = \frac{Q_0 R_0^2}{k_f (T_w - T_1)}$	Heat generation parameter	Strength of internal heat source
$S_z = \frac{\sigma_f}{k_f} \frac{R_0^2 E_0^2}{k_f (T_w - T_0)}$	Electrical dissipation parameter	Ohmic heating effect
$U_{hs} = \frac{\zeta \varepsilon E_0}{\mu_0 U_0}$	Helmholtz-Smoluchowski velocity	Electro-osmotic velocity scale

Table 2. Range of the key influential parameters [16, 29–34]

Non-dimensional parameters	Selected rang of parameters
Magnetic parameter (M)	1–11
Pressure gradient parameter (B_1)	0–2
Heat generation parameter (Q))	0–11
Brownian motion parameter (N_b)	0–1
Thermophoresis parameter (N_t)	0–1
Eckert number (Ec)	0–5
Jeffrey fluid parameter (λ_1)	0–1
Brinkman number (Br)	0–0.4
Temperature ratio Parameter (ω)	0.1–10

The succeeding study considers two specific hypotheses: $\delta \ll 1$, signifying that the stenosis elevation parameter is much less than one, and $\varepsilon = O(1)$, showing that the vessel's aspect ratio is approximately equal to one in magnitude. Imposing these constraints, equations (4) through (9) become:

$$\frac{\partial w}{\partial z} = 0, \tag{16}$$

$$-\left(\frac{\partial p}{\partial r}\right) = 0, \tag{17}$$

$$\left(\frac{\rho_{tethnf}}{\rho_f}\right) \mathrm{Re}\left[\frac{\partial w}{\partial t}\right] = -\frac{\partial p}{\partial z} + \frac{1}{(1+\lambda_1)} \frac{1}{r} \frac{\partial}{\partial r}\left[\frac{\mu_{tethnf}}{\mu_f} r \frac{\partial w}{\partial r}\right]$$

$$+ \frac{(\rho\gamma)_{tethnf}}{(\rho\gamma)_f} Gr\theta - \left(\frac{\sigma_{tethnf}}{\sigma_f}\right) M^2 w + G(t) \tag{18}$$

$$\left(\frac{(\rho C_P)_{tethnf}}{(\rho C_P)_f}\right)\mathrm{Re}\left[\frac{\partial\theta}{\partial t}\right]=\frac{1}{Pr}\left(\frac{k_{tethnf}}{k_f}\right)\left[\frac{\partial^2\theta}{\partial r^2}+\frac{1}{r}\frac{\partial\theta}{\partial r}\right]+\frac{N_b}{Pr}\left[\left(\frac{\partial\sigma}{\partial r}\frac{\partial\theta}{\partial r}\right)\right]+N_t\left[\left(\left(\frac{\partial\theta}{\partial r}\right)^2\right)\right]$$

$$+\frac{\sigma_{tethnf}}{\sigma_f}\left[EcM^2w^2+\frac{S_z+Q}{Pr}\right]+\frac{\mu_{tethnf}}{\mu_f}\frac{1}{(1+\lambda_1)}Ec\left[\left(\frac{\partial w}{\partial r}\right)^2\right] \tag{19}$$

$$ReSc\left[\frac{\partial\sigma}{\partial t}\right]=\left[\frac{\partial^2\sigma}{\partial r^2}+\frac{1}{r}\frac{\partial\sigma}{\partial r}\right]+\frac{N_t}{N_b}\left[\frac{\partial^2\theta}{\partial r^2}+\frac{1}{r}\frac{\partial\theta}{\partial r}\right]-Sc\xi\sigma, \tag{20}$$

$$ReSc\frac{\partial\chi}{\partial t}=\frac{\partial^2\chi}{\partial r^2}+\frac{1}{r}\frac{\partial\chi}{\partial r}-Pe\sigma_1\left(\frac{\partial\chi}{\partial r}\frac{\partial\sigma}{\partial r}+(\sigma_1+\chi)\frac{\partial^2\sigma}{\partial r^2}\right). \tag{21}$$

The electro-osmosis equation in its dimensionless representation is:

$$\frac{\partial^2\Phi}{\partial r^2}+\frac{1}{r}\frac{\partial\Phi}{\partial r}=q^2\Phi. \tag{22}$$

The Reynolds viscosity model is expressed as:

$$\mu_f(\theta)=\mu_0e^{-\beta_0\theta}=\mu[1-\beta_0\theta]\text{ where }\beta_0\ll1, \tag{23}$$

so,

$$\mu_{tethnf}=\frac{\mu_0(1-\beta_0\theta)}{(1-\phi_1)^{2.5}(1-\phi_2)^{2.5}(1-\phi_3)^{2.5}(1-\phi_4)^{2.5}}. \tag{24}$$

The geometric configuration expressed in a dimensionless form is:

$$R(z)=\begin{cases}[1-2\delta(z-2d)]\,\Omega(t), & d\le z\le d+1/2,\\ \left[1+\frac{\delta}{5}\left(\frac{4}{5}-\frac{11}{5}d\right)\right]\Omega(t), & d+\frac{1}{2}\le z\le d+\frac{3}{2},\\ [1+2\delta(z-d-1)]\,\Omega(t), & d+\frac{3}{2}\le z\le d+2,\\ \left[1+\delta\sin\left(\pi(z-d)\right)\right]\Omega(t), & d+2\le z\le d+3,\\ R_0\Omega(t), & \text{otherwise.}\end{cases} \tag{25}$$

Separating the pressure gradient into its non-fluctuating (continuous) and fluctuating (pulsatile) components is possible. The two components are defined as follows:

$$-\frac{\partial p}{\partial z} = A_0 + A_1 \cos(w_p t), \quad t > 0,$$
$$w_p = 2\pi f_p, \tag{26}$$

where A_0, A_1, and f_p signify the amplitude of the pulsatile component, steady state component, and frequency of the heart pulse, respectively.

By introducing dimensionless variables, the pressure gradient equation is transformed:

$$-\frac{\partial p}{\partial z} = B_1 [1 + e\cos(c_1 t)], \tag{27}$$

where

$$e = \frac{A_1}{A_0}, \quad B_1 = \frac{A_0 R^2}{\mu_f U_0}, \; c_1 = \frac{2\pi R_0 f_p}{U_0}. \tag{28}$$

2.3 *Transformation into a rectangular coordinate system*

Nevertheless, to apply the computational method, the geometry under consideration must be mapped to a rectangular domain through the transformation $x = r/R(z)$. Upon applying this transformation and incorporating the nanofluid properties provided in Table 2, Equations (17)–(22) are transformed to [33]:

$$\frac{\rho_{tethnf}}{\rho_f} Re \left[\frac{\partial w}{\partial t}\right] = B_1 [1 + e\cos(c_1 t)] + \left[\left(\frac{(\rho\gamma_T)_{tethnf}}{(\rho\gamma_T)_f}\right)\right] Gr_T \theta - \frac{\sigma_{thnf}}{\sigma_f} M^2 w$$
$$+ \frac{1}{R^2}\left(\frac{(1-\beta_0\theta)}{(1-\phi_1)^{2.5}(1-\phi_2)^{2.5}(1-\phi_3)^{2.5}(1-\phi_4)^{2.5}}\right)\left(\frac{1}{1+\lambda_1}\right)\left[\left(\frac{\partial^2 w}{\partial x^2} + \frac{1}{x}\frac{\partial w}{\partial x}\right)\right] + G(t)$$
$$- \frac{\beta_0}{R^2(1+\lambda_1)(1-\phi_1)^{2.5}(1-\phi_2)^{2.5}(1-\phi_3)^{2.5}(1-\phi_4)^{2.5}}\frac{\partial\theta}{\partial x}\frac{\partial w}{\partial x} + \left[\left(\frac{(\rho\gamma_C)_{tethnf}}{(\rho\gamma_C)_f}\right)\right] Gr\,\theta, \tag{29}$$

$$\left[\left(\frac{(\rho C_p)_{tethnf}}{(\rho C_p)_f}\right)\right] RePrR^2 \left[\frac{\partial\theta}{\partial t}\right] = \frac{k_{tethnf}}{k_f}\left[\frac{\partial^2\theta}{\partial x^2} + \frac{1}{x}\frac{\partial\theta}{\partial x}\right] + N_b\left[\left(\frac{\partial\sigma}{\partial x}\right)\left(\frac{\partial\theta}{\partial x}\right)\right]$$
$$+ \left(\frac{(1-\beta_0\theta)}{(1-\phi_1)^{2.5}(1-\phi_2)^{2.5}(1-\phi_3)^{2.5}(1-\phi_4)^{2.5}}\right)\left(\frac{1}{1+\lambda_1}\right) EcPr\left[\left(\frac{\partial w}{\partial x}\right)^2\right]$$

$$+N_t\left[\left(\frac{\partial\theta}{\partial x}\right)^2\right]+\frac{\sigma_{tethnf}}{\sigma_f}R^2\left[PrEcM^2w^2+S_z+Q\right], \tag{30}$$

$$ReLeR^2\left[\frac{\partial\sigma}{\partial t}\right]=\left[\frac{\partial^2\sigma}{\partial x^2}+\frac{1}{x}\frac{\partial\sigma}{\partial x}\right]+\frac{N_t}{N_b}\left[\frac{\partial^2\theta}{\partial x^2}+\frac{1}{x}\frac{\partial\theta}{\partial x}\right]-Sc\xi\sigma, \tag{31}$$

$$ReScR^2\frac{\partial\chi}{\partial t}=\frac{\partial^2\chi}{\partial x^2}+\frac{1}{x}\frac{\partial\chi}{\partial x}-Pe\Omega\left(\frac{\partial\chi}{\partial x}\frac{\partial\sigma}{\partial x}+(\Omega+\chi)\frac{\partial^2\chi}{\partial x^2}\right), \tag{32}$$

$$\frac{\partial^2\Phi}{\partial x^2}+\frac{1}{x}\frac{\partial\Phi}{\partial x}=R^2q^2\Phi. \tag{33}$$

Furthermore, the associated boundary conditions are:

$$w=w_B,\ \theta=1,\ \sigma=1,\ \chi=1 \text{ at } x=1, \tag{34}$$

$$\frac{\partial w}{\partial x}=0,\ \frac{\partial\theta}{\partial x}=0,\ \frac{\partial\sigma}{\partial x}=0,\ \frac{\partial\chi}{\partial x}=0 \text{ at } x=0. \tag{35}$$

The initial conditions are:

$$w=0,\ \theta=0,\ \sigma=0,\ \chi=0 \text{ at } t=0. \tag{36}$$

The primary haemodynamic parameters of interest can be characterised as the volumetric flow rate, the wall shear stress, and the resistance impedance, with their respective equations provided in [33]:

$$Q_1=2\pi\int_0^R wrdr, \tag{37}$$

$$\tau_s=-\left(\frac{\partial w}{\partial r}\right)_{r=R}, \tag{38}$$

$$\Lambda=\frac{L\left(\frac{\partial p}{\partial z}\right)}{Q}. \tag{39}$$

Similarly, the formulations for the volumetric flow rate, wall shear stress, and resistance impedance, as shown by equations (37)–(39), can be articulated as follows by employing the transformation $x=\frac{r}{R(z)}$.

$$Q_1=2\pi R^2\int_0^1 wxdx, \tag{40}$$

$$\tau_s = -\frac{1}{R}\left(\frac{\partial w}{\partial x}\right)_{x=1}, \tag{41}$$

$$\Lambda = \frac{L\left(\frac{\partial p}{\partial z}\right)}{Q}. \tag{42}$$

2.4 *Entropy generation and Bejan number*

Entropy and energy dissipation for fluid flow are strongly related notions. Blood flow through blood vessels is modulated by the endothelium, a sheet-like layer of cells that acts as a natural barrier to blood flow. This inhibitory effect is due to the viscosity of blood and leads to a transformation of kinetic energy into heat. The differences in entropy and the flow patterns might be used for diagnostic purposes. The analysis of the influence of entropy on blood flow haemodynamics in stenosed, bifurcated arteries for different factors is given by [16] as:

$$E_g = \frac{k_f}{T_1^2}\left(\frac{k_{tethnf}}{k_f} + Nr\right)\left(\frac{\partial T}{\partial r}\right)^2 + \frac{\mu_{tethnf}}{T_1}\left(\frac{1}{1+\lambda_1}\right)\left(\frac{\partial w}{\partial r}\right)^2 + \frac{\sigma_{tethnf}\, B_0^2}{T_1}\left(u^2 + w^2\right). \tag{43}$$

In this context, the first term represents thermally irreversible processes, the second term indicates viscous irreversibility, and the third term describes Joule heating irreversibility.

The non-dimensionalised form of equation (43) is:

$$N_s = \frac{k_{tethnf}}{k_f}\left(\frac{\partial \theta}{\partial r}\right)^2 + \frac{\mu_{tethnf}}{\mu_0}\left(\frac{1}{1+\lambda_1}\right)\frac{Br}{\omega}\left(\frac{\partial w}{\partial r}\right)^2 + \frac{\sigma_{tethnf}}{\sigma_f}\frac{M^2 Br}{\omega}w^2. \tag{44}$$

Where $N_s = \frac{T_1^2 R_0^2}{k_f (T_w - T_1)^2} E_g$ signifies the dimensionless entropy generation.

This reformulation indicates the influence of viscosity, radiation and Joule heating on entropy generation in the system:

$$\begin{aligned} N_s =& \frac{k_{tethnf}}{k_f}\frac{1}{R^2}\left(\frac{\partial \theta}{\partial x}\right)^2 + \frac{\sigma_{tethnf}}{\sigma_f}\frac{M^2 Br}{\omega}w^2 \\ &+ \frac{1}{\omega R^2}\left(\frac{(1-\beta_0\theta)}{(1-\phi_1)^{2.5}(1-\phi_2)^{2.5}(1-\phi_3)^{2.5}(1-\phi_4)^{2.5}}\right)\left(\frac{1}{1+\lambda_1}\right)\left(\frac{\partial w}{\partial x}\right)^2. \end{aligned} \tag{45}$$

The Bejan number is defined as

$$Be = \frac{\frac{k_{tethnf}}{k_f}\frac{1}{R^2}\left(\frac{\partial \theta}{\partial x}\right)^2}{N_s}. \tag{46}$$

In Table 3, thermophysical properties of the blood, Cu, Au, TiO_2, and Al_2O_3 are displayed. The thermophysical parameters of tetra-hybrid nanofluid are given in Table 4 respectively.

Table 3. Thermophysical characteristics of nanoparticles and blood [35]

Thermophysical properties	Density ρ(kg/m^3)	Heat capacitance C_P (J/kg K)	Electrical conductivity	Thermal conductivity k(W/mK)	Thermal expansion $\gamma \times 10^{-5}$(K^{-1})
Blood	1063	3594	0.492	0.667	0.18
Copper(s_1)	8933	385	400	5.96×10^7	1.67
Aluminum Oxide (s_2)	4970	765	40	4.1×10^6	0.85
Titanium Oxide (s_3)	4250	686	8.96	2.4×10^6	0.90
Gold (s_4)	19,320	129	314	4.7×10^7	1.4

Table 4. Thermophysical formulation for tetra-hybrid nanofluid [16]

Properties	Properties
Density	$\rho_{tethnf} = \left[(1-\phi_1)\left\{(1-\phi_2)(1-\phi_3)\left[(1-\phi_4)\rho_f + \phi_4\rho_{s_4}\right] + \phi_3\rho_{s_3} + \phi_2\rho_{s_2}\right\} + \phi_1\rho_{s_1}\right]$
Dynamic viscosity	$\mu_{tethnf} = \frac{\mu_f}{(1-\phi_1)^{2.5}(1-\phi_2)^{2.5}(1-\phi_3)^{2.5}(1-\phi_4)^{2.5}}$
Heat capacity	$(\rho C_p)_{tethnf} = \left[(1-\phi_1)\left\{(1-\phi_2)(1-\phi_3)\left[(1-\phi_4)(\rho C_p)_f + \phi_4(\rho C_p)_{s4}\right] + \phi_3(\rho C_p)_{s3} + \phi_2(\rho C_p)_{s2}\right\} + \phi_1(\rho C_p)_{s1}\right]$
Thermal expansion	$\gamma_{thnf} = [(1-\phi_1)\left[(1-\phi_2)(1-\phi_3)\left\{(1-\phi_4)\gamma_f + \phi_4\gamma_{s_4}\right\} + \phi_3\gamma_{s3} + \phi_2\gamma_{s_2}\right] + \phi_1\gamma_{s_1}$
Thermal conductivity	$\frac{k_{tethnf}}{k_{thnf}} = \frac{k_{s_4}+(n-1)k_f-(n-1)\phi_4(k_f-k_{s_4})}{k_{s_4}+(n-1)k_f+\phi_4(k_f-k_{s_4})}$ where, $\frac{k_{thnf}}{k_{hnf}} = \frac{k_{s_3}+(n-1)k_f-(n-1)\phi_3(k_f-k_{s_3})}{k_{s_3}+(n-1)k_f+\phi_3(k_f-k_{s_3})}$
Electrical conductivity	$\frac{\sigma_{tethnf}}{\sigma_{thnf}} = \frac{\sigma_{s_4}+(n-1)\sigma_f-(n-1)\phi_4(\sigma_f-\sigma_{s_4})}{\sigma_{s_4}+(n-1)\sigma_f+\phi_4(\sigma_f-\sigma_{s_4})}$ where, $\frac{\sigma_{thnf}}{\sigma_{nf}} = \frac{\sigma_{s_3}+(n-1)\sigma_f-(n-1)\phi_3(\sigma_f-\sigma_{s_3})}{\sigma_{s_3}+(n-1)\sigma_f+\phi_3(\sigma_f-\sigma_{s_3})}$

3. Numerical methodology

3.1 *Finite Difference Method (FDM)*

The coupled, nonlinear, and unsteady momentum, energy, nanoparticle concentration, and microorganism density governing equations are solved using FDM. The radial direction is uniformly discretized over the domain and time integration is performed with a constant step. Spatial derivatives are discretized using central difference approximations, and time is discretized to first-order backward difference. A semi-implicit scheme is used for both numerical stability and computational efficiency. In this method, the momentum equation is handled as an implicit system using Thomas algorithm with respect to viscous diffusion and temporal terms; the other transport equations are computed explicitly point by point with under-relaxation. The mixed formulation enables the handling of the stiff momentum equation sturdily and, at the same time, keeps simple the scalar transport equations. The overall methodology adopted in this study is illustrated in Figure 2.

The radial domain is discretized using N_x evenly spaced grid points separated by the grid spacing Δx. Simulations are integrated in time over the entire simulation period T_{final} with fixed time step Δt. The transient term in the momentum equation is discretized by a first-order backward Euler method, and the first- and second-order spatial derivatives are discretized by the central difference formula.

The radial first derivative is approximated with second-order central differences, while the second derivative is discretized by a standard second-order central difference operator that has been adjusted close to the axis in order to account for symmetry. A Neumann-type symmetry condition is applied at the centerline to prevent singularity, while velocity, temperature, nanoparticle concentration, and microorganism density satisfy a no-slip wall boundary condition.

$$\frac{\partial w}{\partial t} = \frac{w_i^{k+1} - w_i^k}{2\Delta t}, \quad \frac{\partial w}{\partial x} = \frac{w_{i+1}^k - w_{i-1}^k}{2\Delta x}, \quad \frac{\partial \theta}{\partial x} = \frac{\theta_{i+1}^k - \theta_{i-1}^k}{2\Delta x}, \quad \frac{\partial \theta}{\partial t} = \frac{\theta_i^{k+1} - \theta_i^k}{2\Delta t},$$

$$\frac{\partial \sigma}{\partial t} = \frac{\sigma_i^{k+1} - \sigma_i^k}{2\Delta t}, \quad \frac{\partial \sigma}{\partial x} = \frac{\sigma_{i+1}^k - \sigma_{i-1}^k}{2\Delta x}, \quad \frac{\partial \chi}{\partial t} = \frac{\chi_i^{k+1} - \chi_i^k}{2\Delta t}, \quad \frac{\partial \chi}{\partial x} = \frac{\chi_{i+1}^k - \chi_{i-1}^k}{2\Delta x}. \tag{47}$$

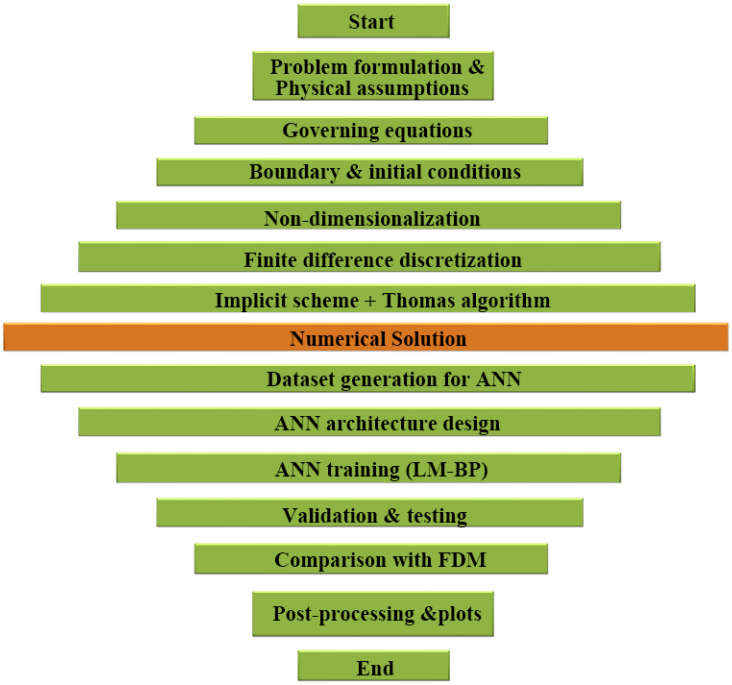


Figure 2. Flowchart of current article

Using Laplacian discretization at $i \geq 2$

$$\begin{aligned} \mathscr{L}[w]_i^{k+1} &= \frac{w_{i+1}^{k+1} - 2w_i^{k+1} + w_{i-1}^{k+1}}{\Delta x^2} + \frac{1}{x_i}\frac{w_{i+1}^{k+1} - w_{i-1}^{k+1}}{2\Delta x}, \quad \mathscr{L}[\theta]_i^{k+1} = \frac{\theta_{i+1}^{k+1} - 2\theta_i^{k+1} + \theta_{i-1}^{k+1}}{\Delta x^2} + \frac{1}{x_i}\frac{\theta_{i+1}^{k+1} - \theta_{i-1}^{k+1}}{2\Delta x}, \\ \mathscr{L}[\sigma]_i^{k+1} &= \frac{\sigma_{i+1}^{k+1} - 2\sigma_i^{k+1} + \sigma_{i-1}^{k+1}}{\Delta x^2} + \frac{1}{x_i}\frac{\sigma_{i+1}^{k+1} - \sigma_{i-1}^{k+1}}{2\Delta x}, \quad \mathscr{L}[\chi]_i^{k+1} = \frac{\chi_{i+1}^{k+1} - 2\chi_i^{k+1} + \chi_{i-1}^{k+1}}{\Delta x^2} + \frac{1}{x_i}\frac{\chi_{i+1}^{k+1} - \chi_{i-1}^{k+1}}{2\Delta x}. \end{aligned} \tag{48}$$

Here $i = 2,\ 3,\ \ldots, N_x - 1$.
Using equations (47) and (48), the governing equations are transformed to the following form:

$$\frac{\rho_{tethnf}}{\rho_f} Re \left[\frac{w_i^{k+1} - w_i^k}{2\Delta t}\right] = B_1 \left[1 + e\cos\left(c_1 t^{k+1}\right)\right] + \left[\left(\frac{(\rho\gamma_T)_{tethnf}}{(\rho\gamma_T)_f}\right)\right] Gr_T \theta_i^k + G\left(t^{k+1}\right)$$

$$+ \frac{1}{R^2}\left(\frac{(1-\beta_0\theta)}{(1-\phi_1)^{2.5}(1-\phi_2)^{2.5}(1-\phi_3)^{2.5}(1-\phi_4)^{2.5}}\right)\left(\frac{1}{1+\lambda_1}\right)\mathscr{L}[w]_i^{k+1}$$

$$+\left[\left(\frac{(\rho\gamma_C)_{tethnf}}{(\rho\gamma_C)_f}\right)\right]Gr\theta_i^k-\frac{\beta_0}{R^2(1+\lambda_1)(1-\phi_1)^{2.5}(1-\phi_2)^{2.5}(1-\phi_3)^{2.5}(1-\phi_4)^{2.5}}$$

$$\frac{\theta_{i+1}^k-\theta_{i-1}^k}{2\Delta x}\frac{w_{i+1}^k-w_{i-1}^k}{2\Delta x}-\frac{\sigma_{thnf}}{\sigma_f}M^2w_i^k, \tag{49}$$

$$\left[\left(\frac{(\rho C_p)_{tethnf}}{(\rho C_p)_f}\right)\right]RePrR^2\left[\frac{\theta_i^{k+1}-\theta_i^k}{2\Delta t}\right]=\frac{k_{tethnf}}{k_f}\mathscr{L}[\theta]_i^{k+1}+N_b\left[\left(\frac{\sigma_{i+1}^k-\sigma_{i-1}^k}{2\Delta x}\right)\left(\frac{\theta_{i+1}^k-\theta_{i-1}^k}{2\Delta x}\right)\right]$$

$$+\left(\frac{(1-\beta_0\theta)}{(1-\phi_1)^{2.5}(1-\phi_2)^{2.5}(1-\phi_3)^{2.5}(1-\phi_4)^{2.5}}\right)\left(\frac{1}{1+\lambda_1}\right)$$

$$EcPr\left[\left(\frac{w_{i+1}^k-w_{i-1}^k}{2\Delta x}\right)^2\right]+N_t\left[\left(\frac{\theta_{i+1}^k-\theta_{i-1}^k}{2\Delta x}\right)^2\right]$$

$$+\frac{\sigma_{tethnf}}{\sigma_f}R^2\left[PrEcM^2w_i^{k2}+S_z+Q\right], \tag{50}$$

$$ReLeR^2\left[\frac{\sigma_i^{k+1}-\sigma_i^k}{2\Delta t}\right]=\mathscr{L}[\sigma]_i^{k+1}+\frac{N_t}{N_b}\mathscr{L}[\theta]_i^{k+1}-Sc\xi\sigma_i^k, \tag{51}$$

$$ReScR^2\frac{\chi_i^{k+1}-\chi_i^k}{2\Delta t}=\mathscr{L}[\chi]_i^{k+1}-Pe\Omega\left(\frac{\sigma_{i+1}^k-\sigma_{i-1}^k}{2\Delta x}\frac{\chi_{i+1}^k-\chi_{i-1}^k}{2\Delta x}+\left(\Omega+\chi_i^k\right)\frac{\chi_{i+1}^k-2\chi_i^k+\chi_{i-1}^k}{\Delta x^2}\right), \tag{52}$$

$$\mathscr{L}[\Phi]_i^{k+1}=R^2q^2\Phi_i^k. \tag{53}$$

3.2 *Artificial Neural Network (ANN)*

The ANN method is used to construct an ANNs-based predictive model for the tetra-hybrid nanofluid for various MHD effects and thermal radiation on mixed convection flow, heat transfer, nanoparticle transport, and microorganism dynamics. The general methodology involves three block steps: data generation, architecture of the ANN and training/testing using a network. The numerical data are obtained by solving coupled governing equations of momentum, energy, nanoparticle concentration, and microorganism density with an implicit Finite Difference Method (FDM) described by the Thomas algorithm. Non-linear thermal radiation, external magnetic field conditions, non-Newtonian fluid, and bioconvective mechanisms are considered in the model.

For network training, the Levenberg-Marquardt backpropagation algorithm is chosen for its quick convergence and strong ability to address nonlinear regression problems consisting of one non-dimensional parameter as input, 10 hidden layers, and 12 output layers. The governing dimensionless parameters are the features of the input layer, and the selected physical response from numerical simulations is predicted in the output layer. Due to fast convergence in nonlinear regression, the Levenberg-Marquardt backpropagation algorithm was used for training. To ensure accuracy and reduce

overfitting, the dataset was randomly split into 70% training, 15% validation, and 15% testing subsets. The predictive performance of the ANN model is examined in terms of statistical measurements, including correlation coefficient, mean squared error, and absolute error. The close parity of ANN forecasts with numerical FDM computations confirms that the proposed ANN technique is an efficient predictive model for stagnant and convective diffusion in MHD-involved tetra-hybrid nanofluid bioconvection, addressing prospective applications in biotechnology and thermal industries. Figures 3 and 4 show the ANN structure and structure of current problem.

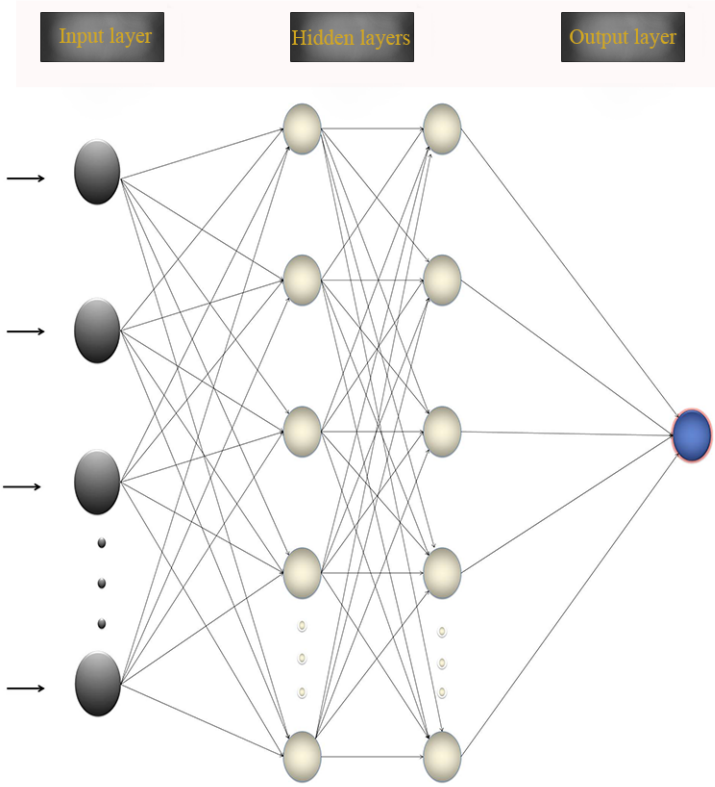


Figure 3. ANN structure

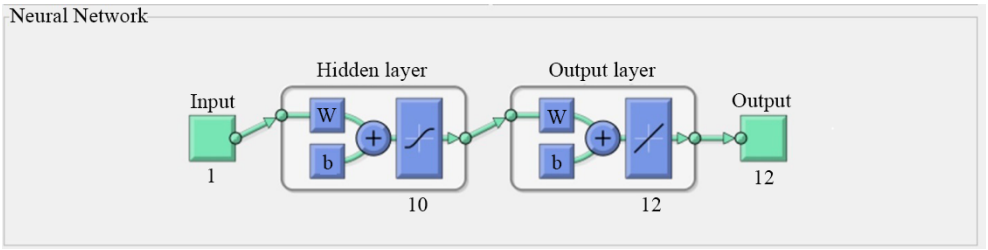


Figure 4. ANN structure of current problem

The output of the neuron for the input t_k is given by

$$v_k = \sum_{i=1}^{k} w_i t_i - \gamma_i \,. \tag{54}$$

The sigmoid activation function is given by

$$\chi(v_i) = \frac{1}{1+e^{-(w_i t_i - \gamma_i)}}. \tag{55}$$

The accuracy of the ANN is quantified using the Mean Squared Error (MSE), the regression coefficient R^2, and the Absolute Error (AE), which are defined as follows:

$$MSE = \frac{1}{i}\sum_{j=1}^{i}(z_j - \widehat{z}_j)^2, \tag{56}$$

$$1 - R^2 = \frac{\sum_{j=1}^{i}(\widehat{z}_j - \overline{x}_j)^2}{\sum_{j=1}^{i}(z_j - \widehat{z}_j)^2}, \tag{57}$$

$$AE = \left|z_j - \widehat{z}_j\right|, \; i = 1,2,3,\ldots,k. \tag{58}$$

4. Validation of numerical scheme

A grid independence study and a time-step sensitivity analysis were performed prior to conducting the main simulations in order to ensure that the proposed semi-implicit finite difference scheme used with the Thomas algorithm was accurate, stable, and numerically robust. For this, two representative output quantities were selected: the dimensionless flow rate Q_1 and the wall shear rate τ_s, as both are physically relevant indicators of the hemodynamic response and depend directly on how well discretization has been done.

To study the spatial convergence of the numerical solution, the computational direction was solved with different numbers of grid points such as $N_x = 301,\ 351,\ 401$ and 451. Table 5 shows the values of Q_1, and τ_s. The flow rate Q_1 converges to the same value as the grid is refined into finer sizes. More specifically, Q_1 is further increased only from 0.02483517 at $N_x = 301$ to 0.02483616 at $N_x = 451$, or less than a significant total difference of only $\sim 0.004\%$. Similarly, the wall shear rate τ_s changes smoothly and monotonically from 1.278087 to 1.289317 as grid resolution increases, indicating gradual convergence trend also. These outcomes suggest that the numerical solution is hardly influenced by mesh refinement beyond $N_x = 401$. Especially for the Q_1 difference between the two next finer meshes ($N_x = 401$ and 451), it is very small, indicating that spatial discretization error does not matter much in practice. Thus, the mesh with $N_x = 401$ was chosen as an appropriate trade-off for further simulations between computing time and numerical precision.

Table 5. Grid independence test outcomes

N_x	Q_1 (Flow rate)	τ_s (shear rate)
301	0.02483517	1.278087
351	0.02483564	1.282892
401	0.02483595	1.286503
451	0.02 483616	1.289317

The same time-step sensitivity test was conducted for $\Delta t = 10^{-4}$, 10^{-5}, 10^{-6} and 10^{-7}. The result presented in Table 6 demonstrates that both Q_1 and τ_s converge quickly with increasingly small time steps. The order of the solution changes negligible when changing time steps $\Delta t = 10^{-6}$ and 10^{-7}, confirming both temporal convergence and stability of the semi-implicit scheme. As a result, $\Delta t = 10^{-6}$ was chosen for all calculations.

Table 6. Time-step sensitivity test outcome

Δt	Q_1 (Flow rate)	τ_s (shear rate)
10^{-4}	0.02482335	1.260187
10^{-5}	0.02483297	1.261362
10^{-6}	0.02483393	1.261480
10^{-7}	0.02483403	1.261492

5. Results and discussion

In this section, the graphical outcomes of the governing equations are discussed in detail. Figure 2 shows the flowchart of current article.

5.1 *ANN Analysis*

The velocity profile ANN validation yields quite impressive predictive performance as shown in Figure 5a–e: average convergence of the mean squared error to 7.34048×10^{-09} occurs at epoch 54, and the training status confirms that the convergence is optimal with a close-to-zero gradient and minimal Mu parameter; the error histogram Figure 5c displays an ideal, sharp peak at zero error for all datasets; and the regression Figure 5d exhibits a perfect match between FDM targets and ANN outputs along the ideal fit line. Such a strict validation proves that the ANN surrogate has been able to accurately emulate the complex connection between input parameters and velocity field in such a way as to replicate with very high accuracy the predictions of the FDM solver, making available an accurate and low computational cost model for immediate evaluation and optimization studies of entropy generation in the stenosed artery model.

The ANN validation for the temperature profile Figure 6a–e exhibit superior performance, obtaining a best validation mean squared error of 1.1399×10^{-08} at epoch 279, with training state metrics indicating good convergence over that with a near-zero gradient and minimal Mu value. The error histogram Figure 6c indicates a narrow, perfectly centered error distribution around the zero value for all data sets, and the regression Figure 6d shows a perfect $(R = 1)$ correlation and a tight cluster of points in proximity to an ideal fit line on the function's fit Figure 6e, which indicates that the ANN output temperature targets are coincident with FDM-calculated ones.

Figure 7a–e show the ANN validation for the nanoparticle concentration profile confirms its high-accuracy approximation to the FDM solver, achieving optimal performance with a mean squared error of 1.349×10^{-08} at epoch 137, along with proper training state indicators such as a close-to-zero gradient and a minimal Mu value. The error histogram reveals a perfectly symmetrical, small spread near zero for all training, validation, and test sets, and the regression plots exhibit a perfect $R = 1$ coefficient of correlation with data points along with the ideal fit line in the function fit Figure 7e, indicating there is no bias.

The ANN prediction of the microorganism's density profile has very high accuracy as shown in Figure 8a–e, with the lowest mean square error obtained in validation equal to 2.0747×10^{-09} at epoch 205 and metrics of the training state that confirm an effective derivation through a near-zero gradient and a close-to-zero Mu parameter. The error histogram shows a tight distribution that centers exactly at zero for all datasets, and the regression data versus function fit demonstrates a perfect correlation $(R = 1)$, with the outputs aligning precisely on top of the FDM targets along the ideal fit line, as indicated by the data points.

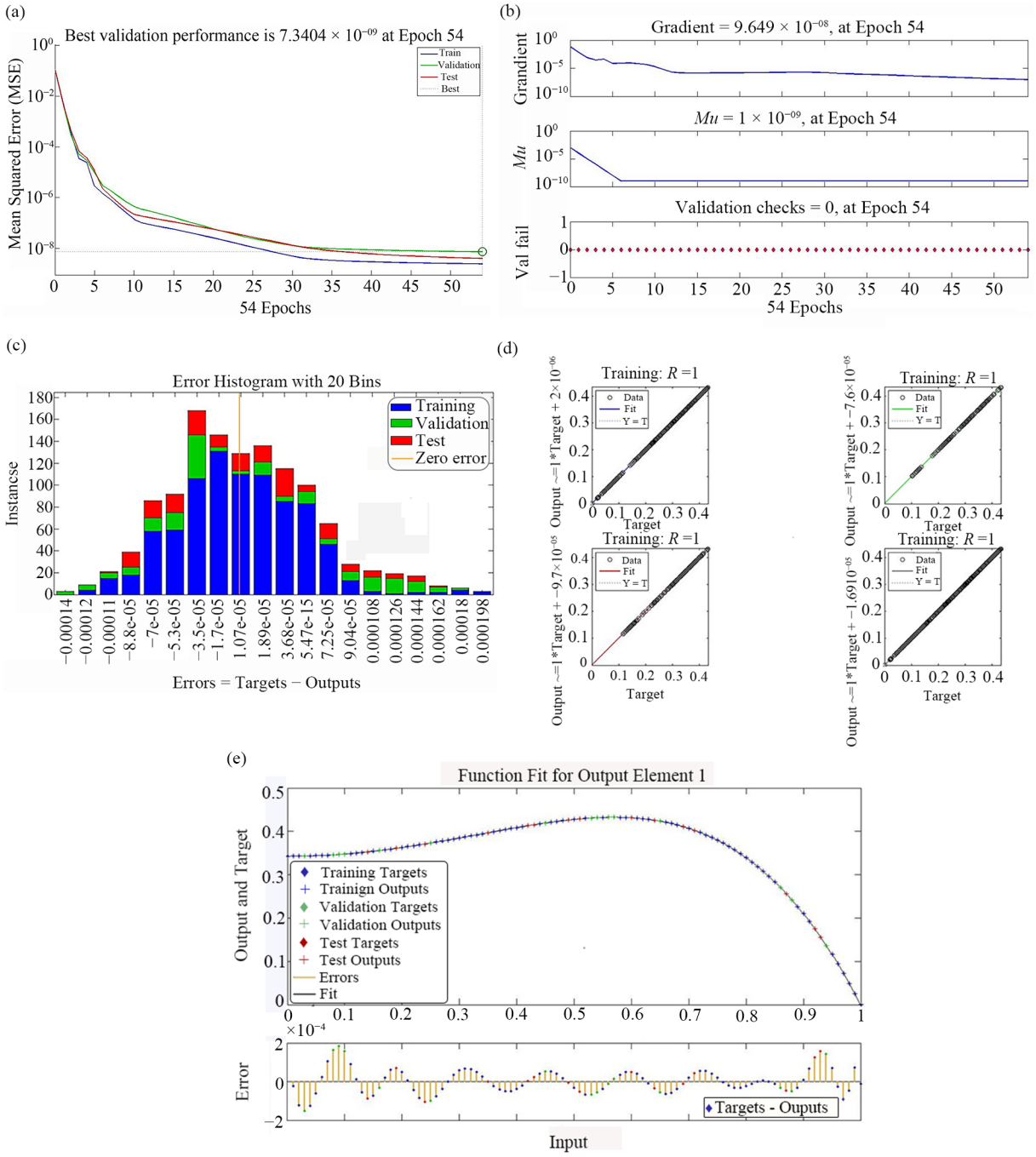


Figure 5. ANN validation for velocity profile (a) Performance plot; (b) Training state; (c) Error histogram; (d) Regression plot; (e) Curve fit

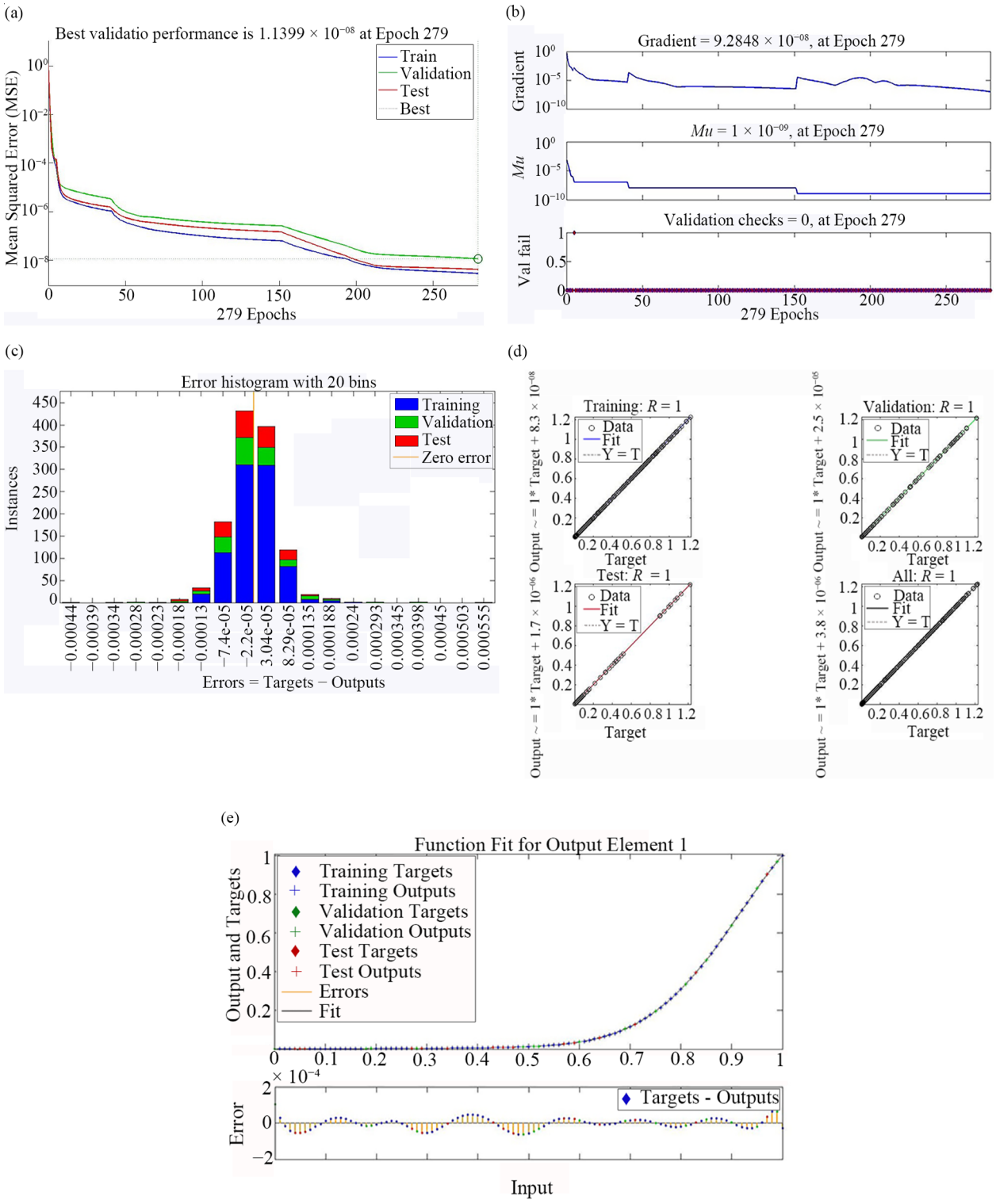


Figure 6. ANN validation for temperature profile (a) Performance plot; (b) Training state; (c) Error Histogram (d) Regression plot (e) Curve fit

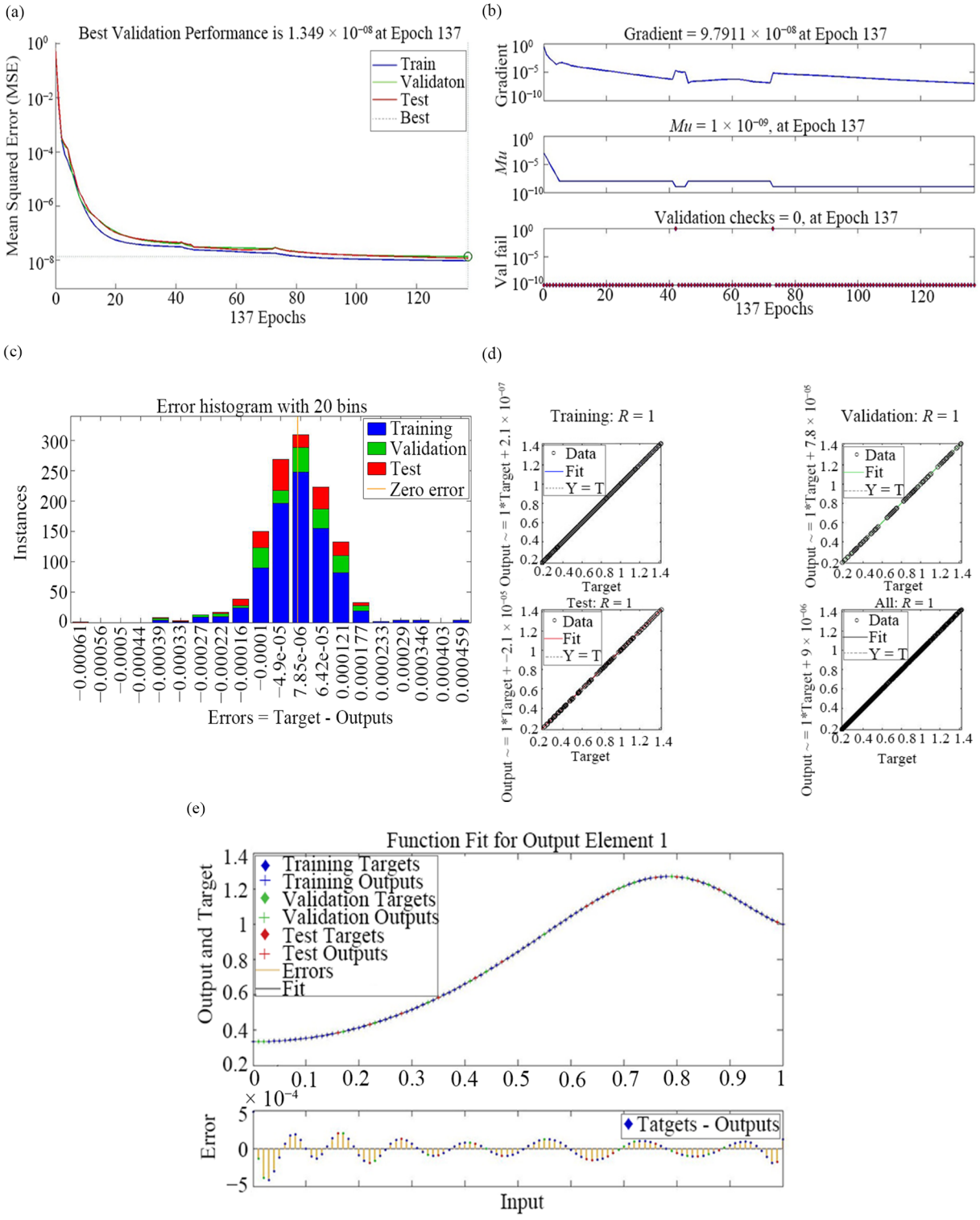


Figure 7. ANN validation for concentration profile (a) Performance plot; (b) Training state; (c) Error histogram; (d) Regression plot; (e) Curve fit

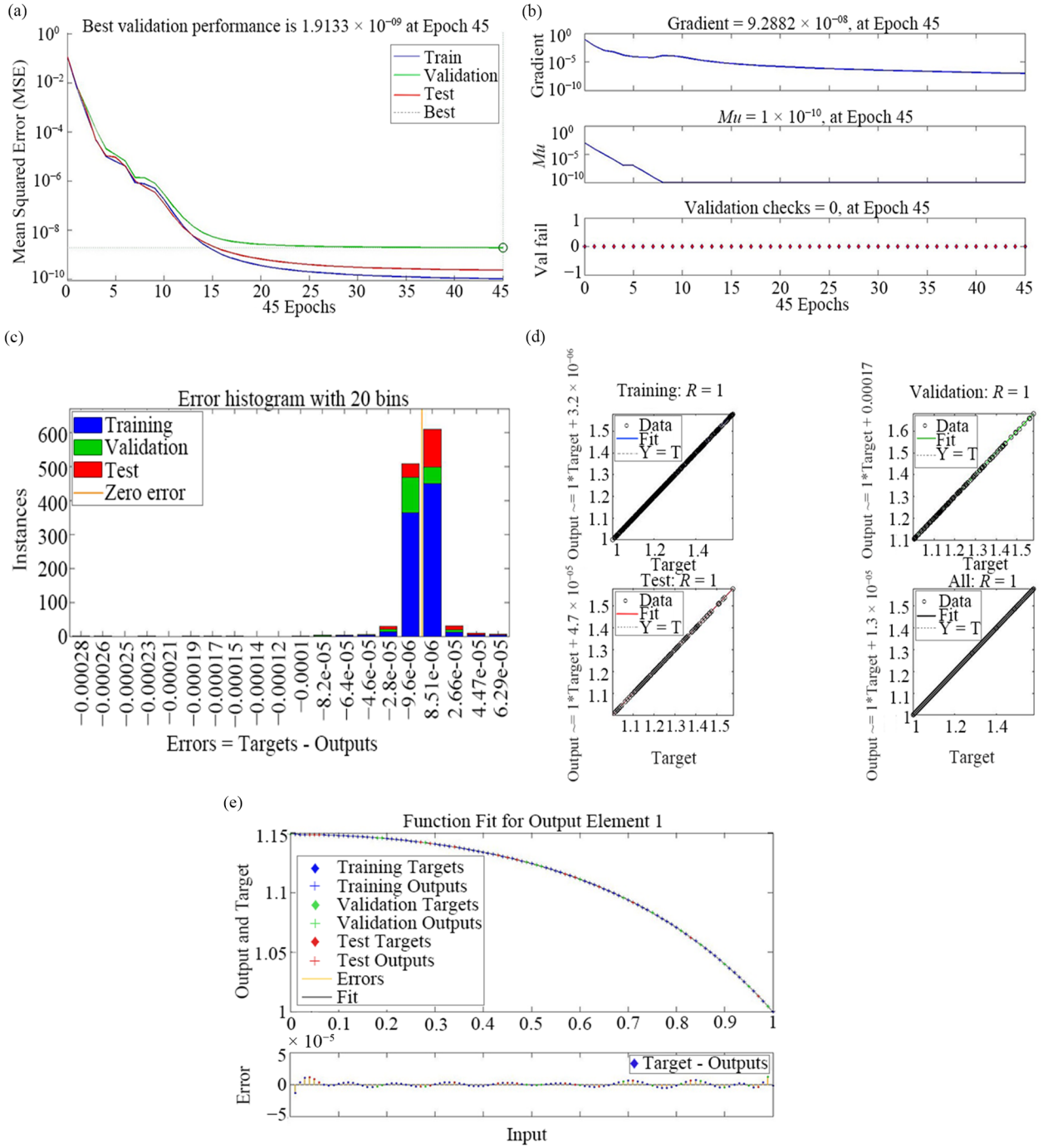


Figure 8. ANN validation for microorganism profile (a) Performance plot; (b) Training state (c); Error histogram (d) Regression plot; (e) Curve fit

Figure 9a–e show that the ANN validation for the entropy generation profile is excellent; the best results are achieved with a mean squared error of 1.0246×10^{-05} at epoch 342, which indicates optimal convergence criteria, including a close-to-zero gradient and a minimal Mu parameter. However, additional epochs and one validation check were required for other profiles. The error histogram reveals an almost Gaussian distribution of errors with a peak close to zero for each data set, while the regression plot also demonstrates perfect correlation $(R = 1)$ as the clusters concentrate near

the reference line on the function graph, which reflects that with good accuracy, the ANN estimates align well with the FDM-calculated entropy targets.

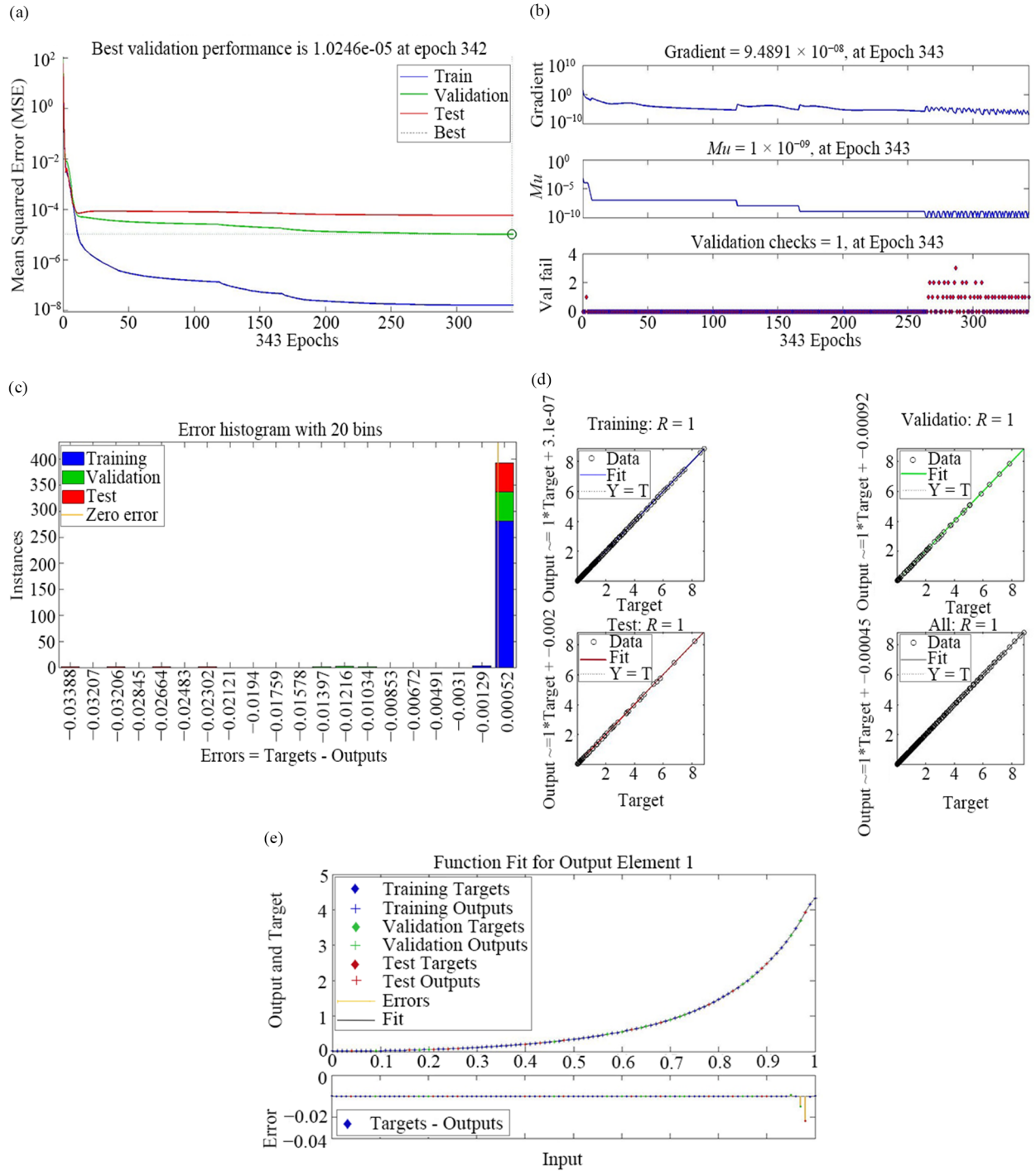


Figure 9. ANN validation for entropy generation (a) Performance plot; (b) Training state (c); Error histogram (d) Regression plot; (e) Curve fit

ANN validation of the Bejan number profile also attests to its high accuracy as shown in Figure 10a–e, with an outstanding best validation performance (2.4568×10^{-08}) recorded at epoch 548, while the training state Figure 10b

reveal a near-zero gradient and minimal *Mu* parameter, both indicating that utmost convergence has been reached despite the higher epoch value. The error histogram Figure 10c displays a very narrow, symmetrical tail distribution of errors that is centered closely around zero for all sets, while the regression Figure 10d shows an ideal correlation ($R = 1$), indicating a perfect fit of the data points on the application graph to the fit line. This suggests that there is no inherent bias in the ANN organization regarding the Bejan number targets provided by FDM prediction. This rigorous validation identifies the ANN surrogate as an extremely accurate and practical model for predicting the Bejan number, which is crucial for assessing heat transfer irreversibility.

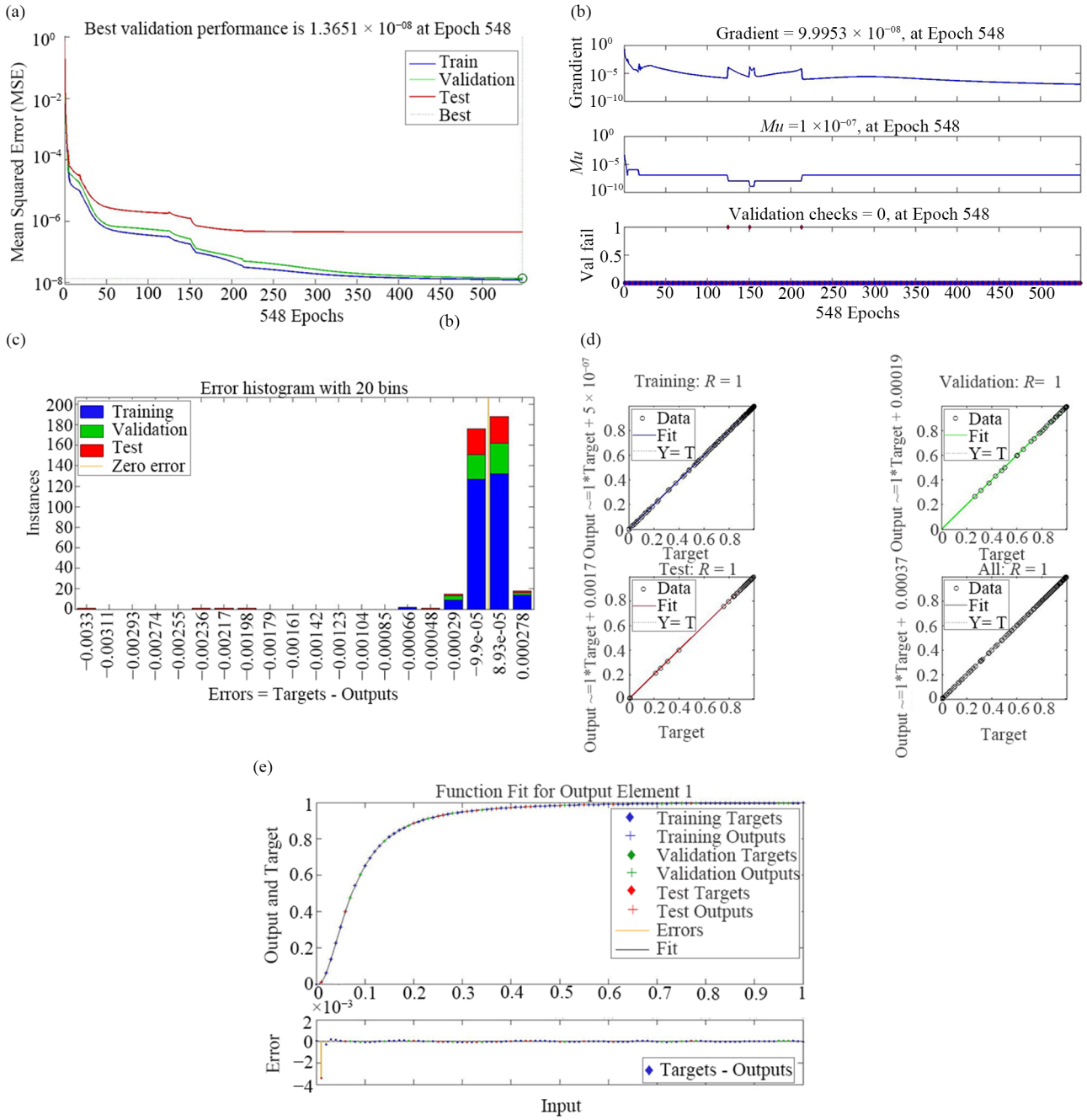


Figure 10. ANN validation for Bejan number (a) Performance plot; (b) Training state; (c) Error histogram; (d) Regression plot; (e) Curve fit

5.2 *Velocity profile*

Figure 11a,b show the effect of velocity profile and its absolute error against distinct λ_1. The effect of λ_1 on the velocity is observed, and it has been seen that as λ_1 increases, the viscosity of Jeffrey fluid enhances its viscoelastic nature. This behavior also has physical implications: a longer relaxation time leads to a reduction of the effective viscosity in regions of high shear, especially around the throat of the stenosis, which makes axial flow smoother and faster. This behavior is indicative of a shear-thinning mechanism that facilitates momentum transport in the core region. From a hemodynamic perspective, such an increase in velocity may cause wall shear stress to increase, which could alter plaque stability and lead to arterial injury risk at stenotic vessels. Figure 12a,b show the influence of velocity profile and its absolute error against distinct M. For large M, the velocity drops significantly because of the Lorentz force induced by the applied magnetic field opposing the flow direction, which is successfully predicted by the ANN surrogate model. This resistive effect raises flow resistance and dampens fluid motion. This damping phenomenon is universal in nature, with various nanofluid configurations further confirming the predominance of magnetohydrodynamic forces. From a biomedical perspective, this mechanism provides a potential non-invasive strategy for controlling flow, whereby externally applied magnetic fields can be used to modulate excessive velocities and relieve hemodynamic stresses in diseased segments of arteries. Figure 13a,b show the effect of velocity profile and its absolute error against distinct B_1. The relationship between the velocity profile and higher values of the pulse pressure gradient parameter B_1 is mainly due to a more intense force oscillation directly increasing the fluid momentum. A greater B_1 translates into larger amplitude of the pulsatile pressure wave, which is the main driver of blood in the arterial system; this enhanced pressure difference better compensates for the opposite viscous and electromagnetic (Lorentz) resistance, leading to an acceleration of flow, where all fluid types clearly feature more pronounced hemodynamic curves whenever B_1 amplitudes are higher. Clinically, increased pulse pressure—which is often associated with stiffness of the arteries as well as hypertension—can lead to extremely high velocities and wall shear stresses, which can enhance the risk of plaque rupture or development of aneurysms. These findings emphasize the loss of vascular health under these pulsatile pressure conditions, focusing on physiological regulation.

The contour and surface plots of the axial velocity profile $w(x,t)$ shown in Figure 14a,b depict overall time-dependent haemodynamics within stenosed and aneurysmal arteries under pulsatile flow conditions and MHD effects. A pair of periodical bands of high and low velocities in time will suggest pulsatility at the time axis in this contour plot, and its radial variation will be like a maximum near to the centre line and a minimum to the walls, with apparent distortions suggesting accelerating velocity at the stenosis region or flow deceleration at the dilation region. The associated 3D surface plot leverages this information to render the time as a landscape showing periodic ridges and troughs and the arched shape of each ridge reflects into a parabolic velocity profile across the vessel radius, with surface waviness and localised depressions correspondingly indicating that in the presence of combining stenosis-aneurysm geometry, significant flow disturbances are induced due to damping effects created by the magnetic field. These visualised traces are crucial diagnostic maps that reveal the specific points in the cardiac cycle and spatial locations where dangerous high-velocity jets or harmful low-velocity recirculation zones occur.

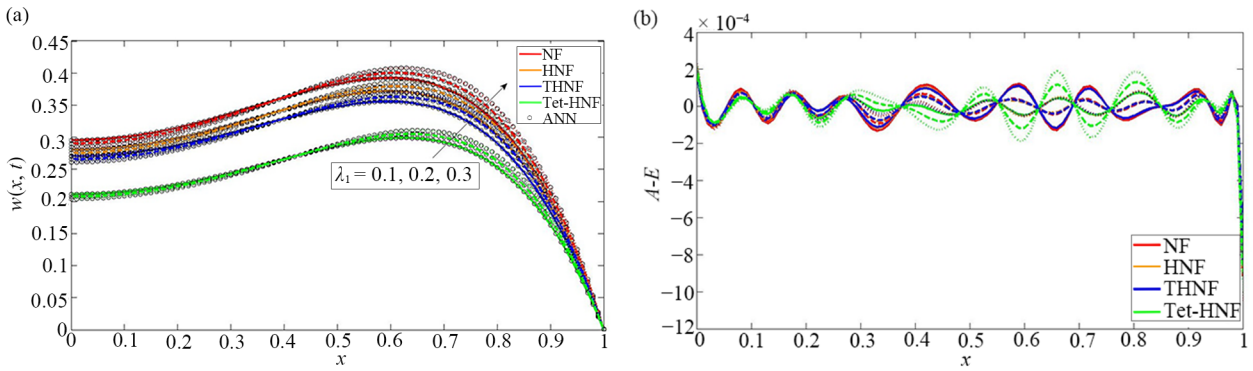


Figure 11. (a) $w(x, t)$ via λ_1; (b) Absolute error

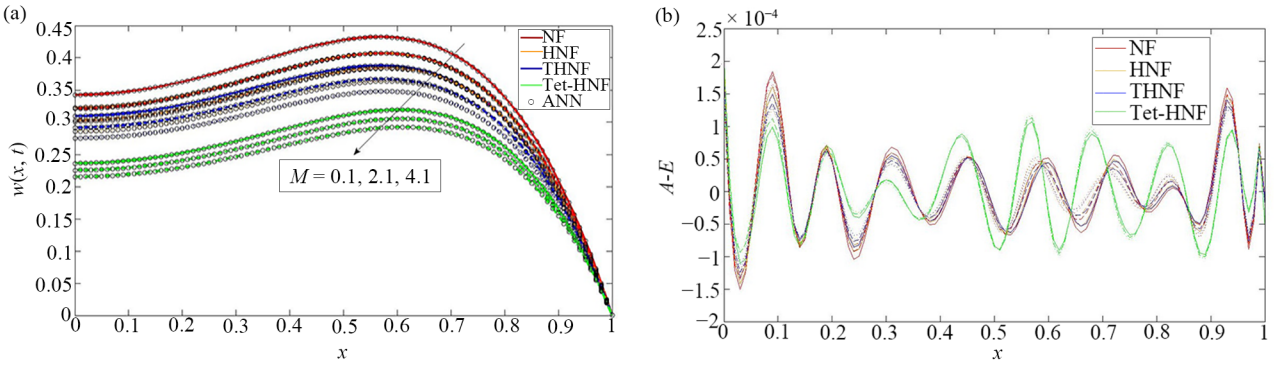


Figure 12. (a) $w(x, t)$ via M; (b) Absolute error

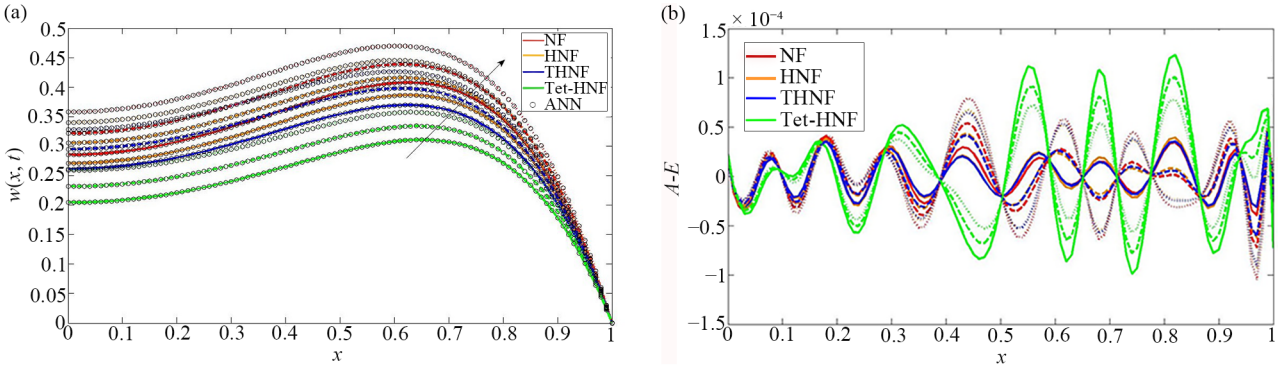


Figure 13. (a) $w(x, t)$ via B_1; (b) Absolute error

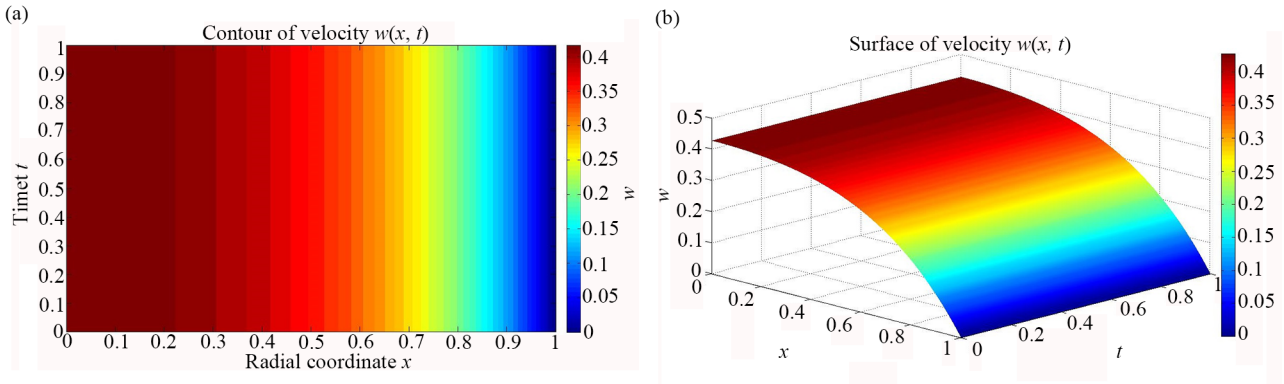


Figure 14. (a) Contour; (b) Surface plot for velocity profile

5.3 *Temperature profile*

Figure 15a,b show the outcome of temperature profile and its absolute error against distinct Ec. The rise in the temperature field profile with a growing Eckert number Ec is a natural consequence of stronger viscous dissipation and Joule's heating effects, and Ec denotes the ratio of kinetic energy to enthalpy difference and a larger value points to more conversion from flow work and electromagnetic work into internal thermal energy. As a result of the fact that induced solvent flow plays as if it is added to an internal source, which becomes quite substantial, especially in high shear regions

such as those near the stenosis throat and under the influence of an applied magnetic field, higher levels of heat are generated for all Nanofluids (NFs) from Nanofluid (NF) to Tet-HNF and this in turn explains why we obtained larger temperature profiles depicted in the figure. In practical biomedical terms, this reveals an important thermal risk in stenosed arteries under abnormal flow conditions where higher values of Ec are associated with either high velocity or strong MHD effects. Figure 16a,b show the consequence of temperature profile and its absolute error against distinct M. The rise of the temperature profile for the higher values of M is due to an increase in Joule heating (Ohmic dissipation), which is essentially caused by electric currents produced due to the applied magnetic field within the nanofluid, as they are electrically conducting. As a result, the resistive dissipation caused by the electric currents corresponds to the conversion of electromagnetic energy into thermal energy, thereby acting as an efficient volumetric heat source. Meanwhile, the Lorentz force opposes the flow velocity and increases fluid friction, which, along with viscous dissipation, further accelerates the temperature rise; it is observed that the temperature curves increase across thinner M for all fluids shown in the Figure. From a biomedical standpoint, the case emphasizes an important heat-related side effect of magnetic field application for therapy. Figure 17a,b show the consequence of temperature profile and its absolute error against distinct Q. Due to having an internal volumetric heat source, an increase in Q causes a simultaneous temperature rise throughout. The extra thermal energy contributes to the heat content within the system, thereby raising the temperature throughout the domain of flow. Physiologically and biophysically, the parameter may also denote metabolic heat production or outside-induced heating mechanisms such as nanoparticle-mediated hyperthermia. The induction of excessive heat might lead to thermal damage, such as protein denaturation and endothelial dysfunction, highlighting the importance of controlled thermal conditions in biomedical applications.

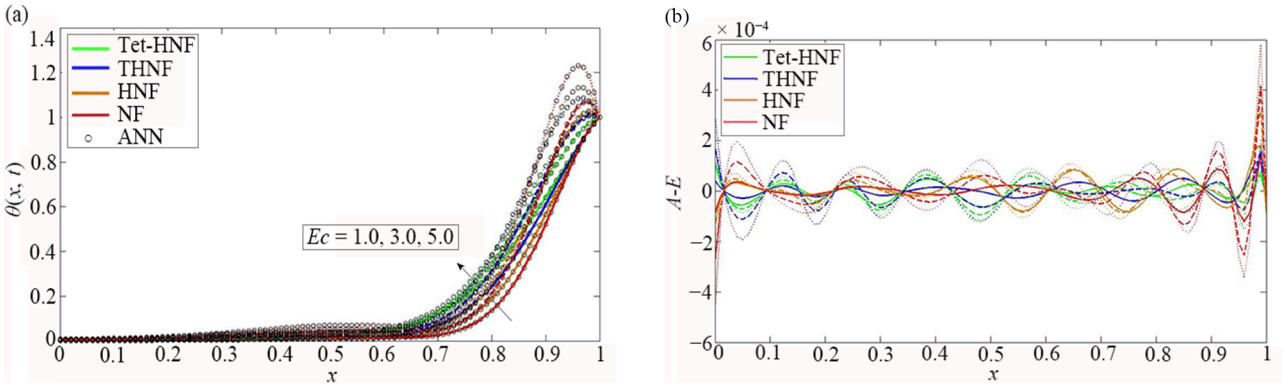


Figure 15. (a) $\theta(x, t)$ via Ec; (b) Absolute error

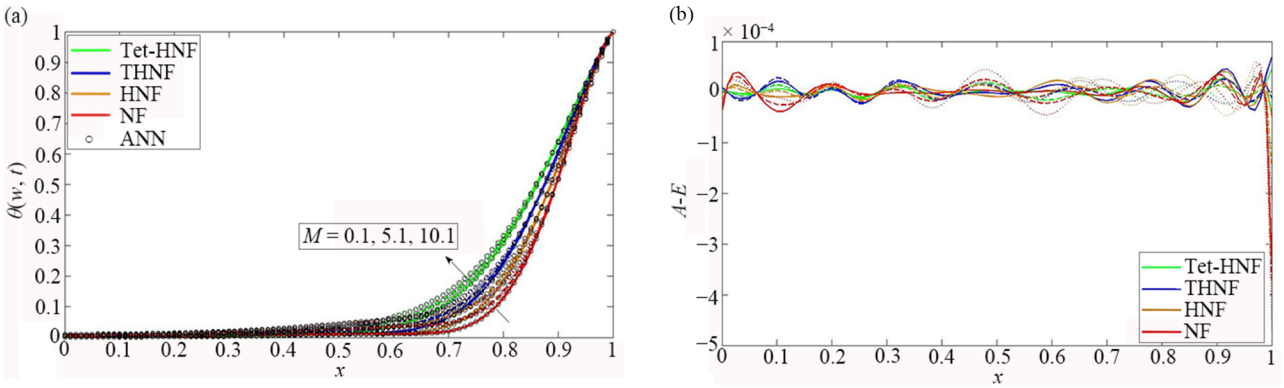


Figure 16. (a) $\theta(x, t)$ via M; (b) Absolute error

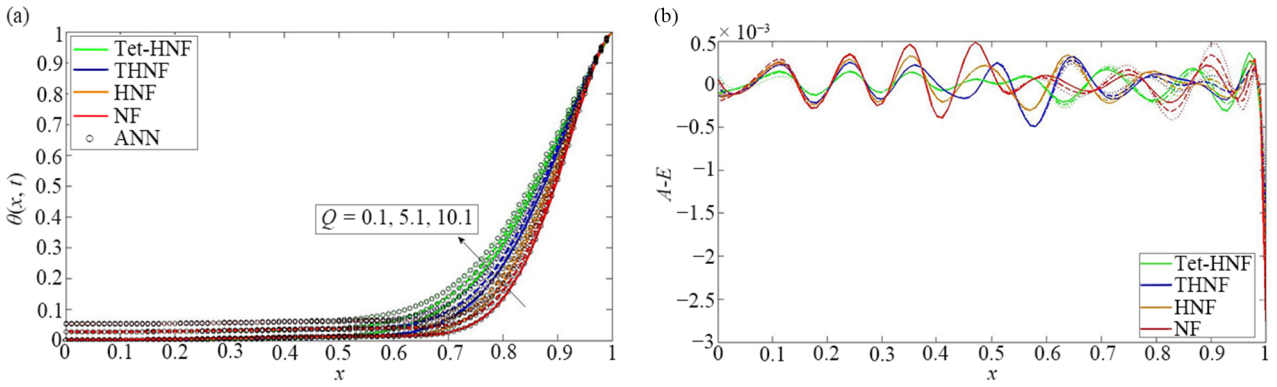


Figure 17. (a) $\theta(x,\ t)$ via Q; (b) Absolute error

The contour and surface plots of the temperature distribution profile $\theta(x,t)$ shown in Figure 18a,b illustrate the intricate spatiotemporal thermal evolution in the artery due to the collective influences of arterial pulsatile flow, viscous heating, and Joule heating, as well as stenosis-aneurysm geometry. The contour Figure 18a illustrates that temperature is modulated both radially and as a function of time; maximum temperatures (brighter contours) are localized in the central core region and pulse-synchronously fluctuate, suggesting thermal peaks coincide with high-velocity phases due to increased viscous dissipation, while rendering these into a 3D surface Figure 18b develops this portrait to reveal topographical features along the time axis marked by periodic thermal spikes and maintains a radial gradient, especially near the vessel center.

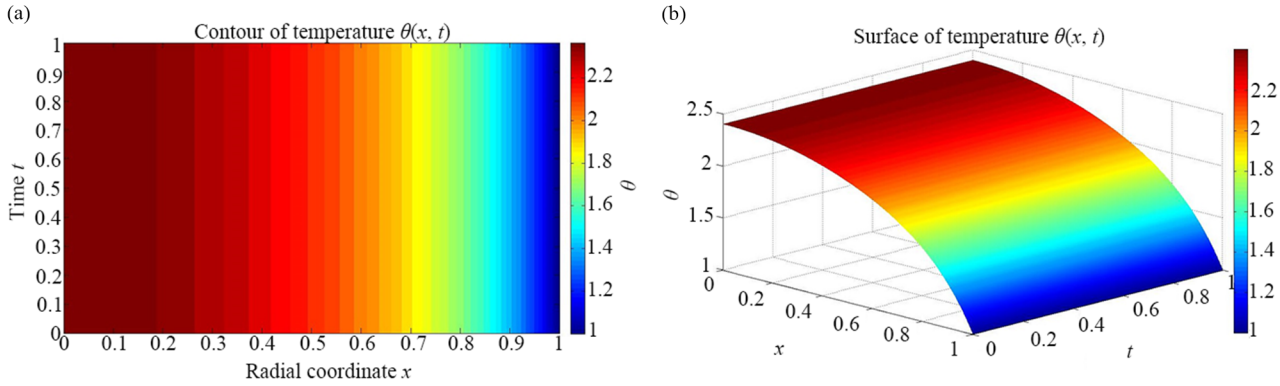


Figure 18. (a) Contour; (b) Surface plot for temperature profile

5.4 *Concentration profile*

Figure 19a,b show the effect of concentration profile and its absolute error against distinct N_t. As the thermophoresis parameter N_t increases, the concentration profile becomes higher since thermophoresis is a phenomenon by which suspended nanoparticles or species move from the hot to colder regions caused by the temperature gradient; hence, an increase in N_t indicates a stronger thermophoretic force transporting particles away from the heated core and wall of the channel towards the cooler central part of the flow that enhances its concentration distribution as shown in the Figure 19a, where each fluid type shows high curves of concentration for greater N values. From a practical biomedical perspective, this mechanism could be crucial for controlling the thermophoretic effect and managing local temperature gradients. Figure 20a,b show the outcome of concentration profile and its absolute error against distinct N_b. The concentration profile diminishes with the increasing of the Brownian motion parameter N_b due to increased contribution from the Brownian diffusion;

i.e., random thermal collision-driven dispersion of nanoparticles brings about more uniform distribution of nanoparticles throughout the fluid domain and reduces any peak for higher N_b values on all fluids. Accordingly, particles drift away from high-concentration regions as illustrated in the Figure 20a. In a biomedical context, this inverse relationship is of vital importance in the development of controlled drug release systems, because too much Brownian motion—intensified by excessive temperature or sufficiently small particle size—can interfere with the specific accumulation of therapeutic nanoparticles at an intended site (such as a stenosis or tumor), thereby reducing the effectiveness of treatment and possibly leading to counterproductive off-target effects; hence, an appropriate balance must be achieved between Brownian diffusion and other transport phenomena such as thermophoresis for obtaining optimal drug delivery and concentration under conditions of precision nanomedicine.

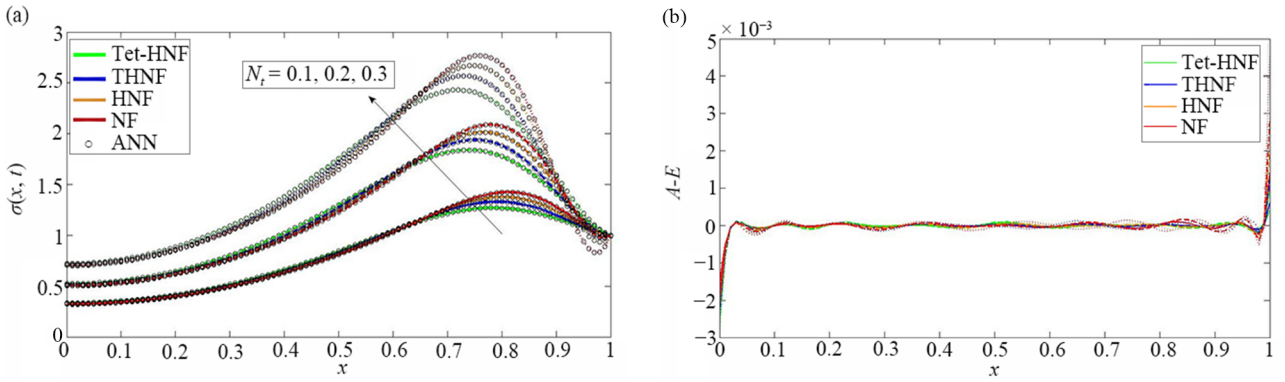


Figure 19. (a) $\sigma(x, t)$ via N_t; (b) Absolute error

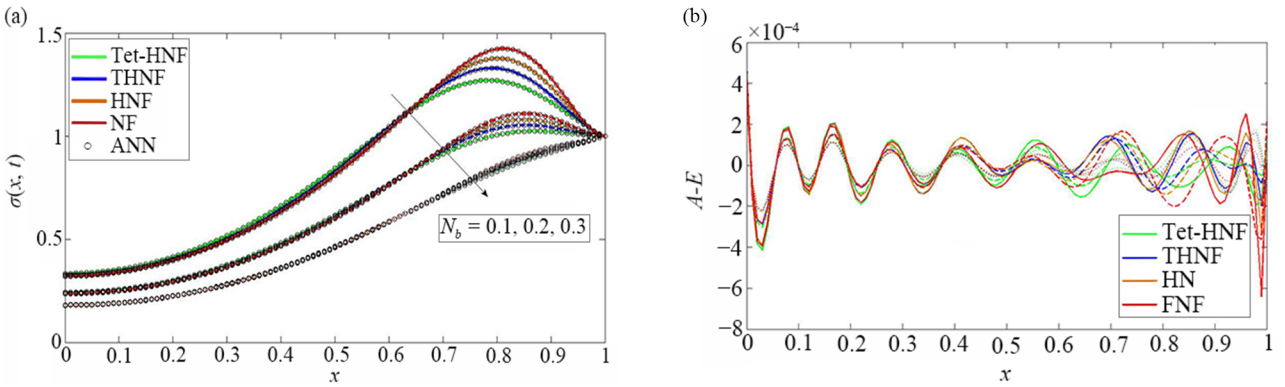


Figure 20. (a) $\sigma(x, t)$ via N_b; (b) Absolute error

The contour and surface plots for the distribution of particle concentration profile $\sigma(x,t)$ shown on Figure 21a,b depict the dynamic and non-uniform distribution of tetra-hybrid nanofluid within a pulsatile flow situation due to the combined effects of Brownian motion, thermophoresis, communication between Brownian diffusion and thermophoresis, and geometric geometry at an arcuate artery. The high and low intensities are concentrated in the central core regions (lighter contours), respectively, that vary periodically in time with slightly adjusting periods, indicating that nanoparticle deposition oscillates with a pulse cycle due to shear-induced dispersion and thermophoretic migration associated with the temperature peaks in the temperature profiles. This spatiotemporal variation is further emphasized in the 3D surface plot Figure 21b, with peaks of concentration corresponding to a series of undulating ridges that repeat periodically across time yet maintain a strong radial gradient, an important feature when evaluating drug delivery efficiency.

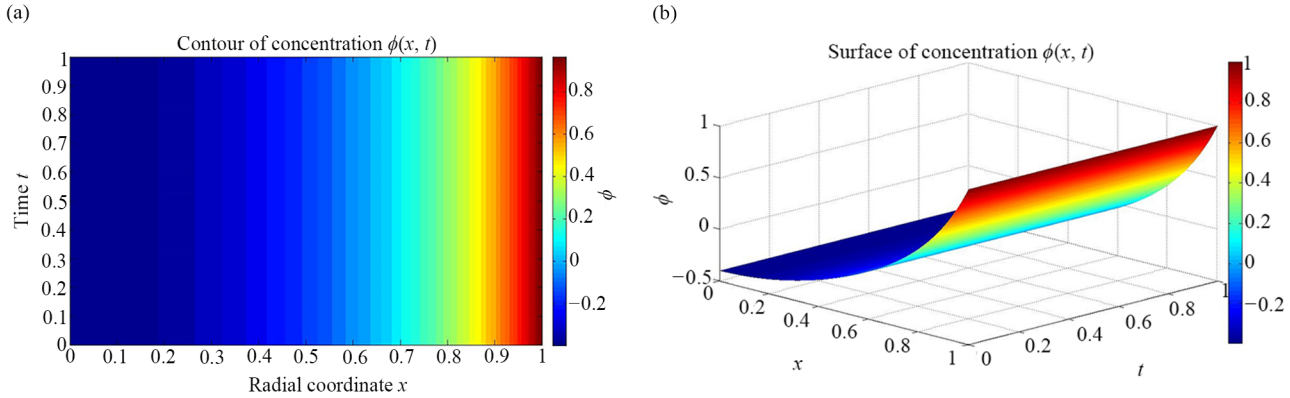


Figure 21. (a) Contour; (b) Surface plot for concentration profile

5.5 *Microoganism profile*

Figure 22a,b show the outcome of microoganism profile and its absolute error against distinct Ω. The microorganism concentration profile improves as the microorganism density ratio parameter Ω increases, because this parameter measures relative concentration and the buoyancy effect of motile microorganisms in the fluid; a higher value results in increased population density or bioconvective strength, which allows microorganisms to be more effectively distributed throughout the domain as they swim along chemical or thermal gradients. This enhanced microbial population density increases bioconvection, resulting in a larger concentration of biomaterials in, e.g., the artery core, as suggested by the trend displayed in the Figure 22a. In real biomedical settings, this dependence is critical to developing and exploiting bioaugmented therapies, where controlling the microorganism density parameter can lead to improved colonization efficacy and distribution of therapeutic microbes at diseased sites but also highlights issues related to regulating potential inflammatory responses or infections in susceptible vascular environments (e.g., stenosed arteries). Figure 23a,b show the consequence of microoganism profile and its absolute error against distinct *Sc*. The microorganism profile is associated with a higher Schmidt number because the Schmidt number *Sc* is defined as the cube of the ratio of momentum diffusivity to mass diffusivity; thus, a larger Schmidt number indicates that viscous effects dominate over dissipation, impairing random motions related to fluid transport. This decrease in mass diffusivity inhibits the ability of the microorganisms to spread and mix throughout the flow (i.e., become dispersed); hence, they localize more and have a lower total concentration profile as indicated by the falling profiles in Figure 23a. In practice, this property is critically important for biomedical processes such as targeted drug delivery to bacteria, where a high effective Schmidt number—resulting from either high viscosity or low motility of the microorganisms—can hinder adequate dispersion of microbes towards infection sites.

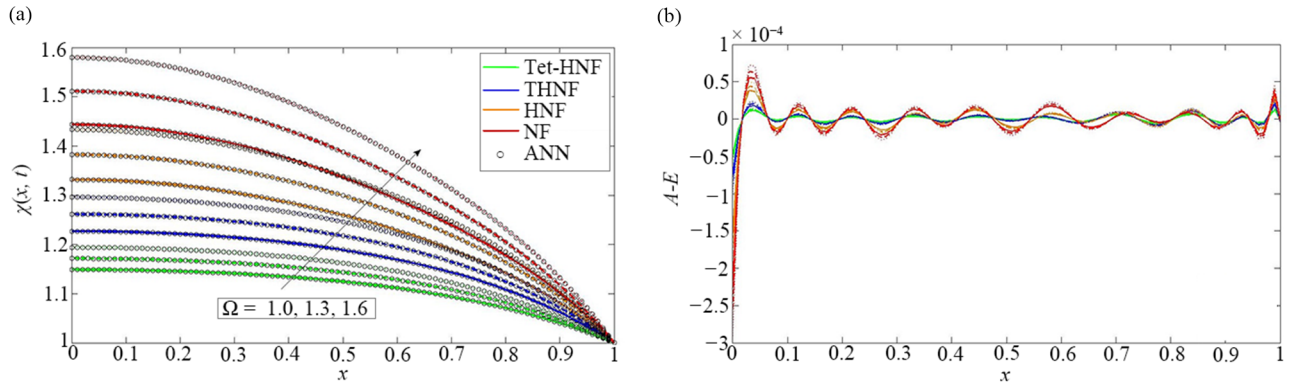


Figure 22. (a) $\chi(x, t)$ via Ω; (b) Absolute error

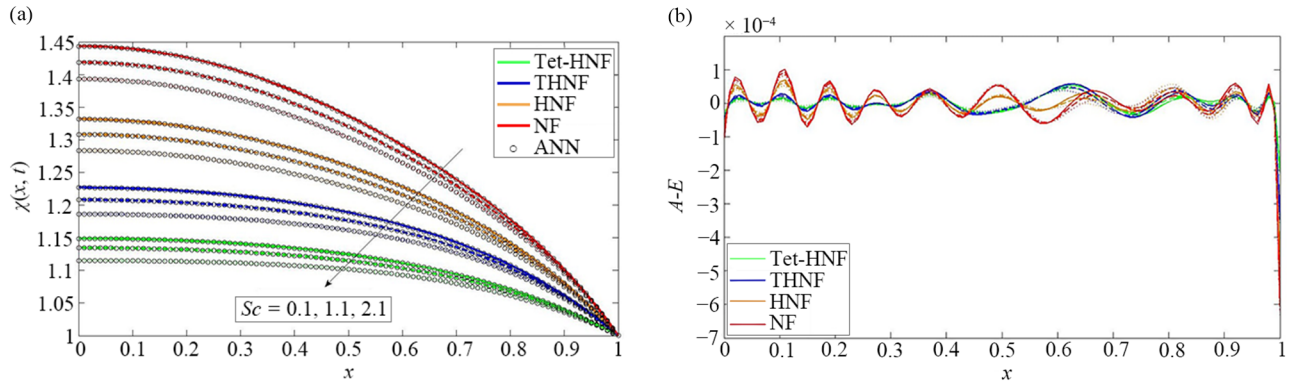


Figure 23. (a) $\chi(x, t)$ via *Sc*; (b) Absolute error

The contour and surface plots for the microorganism density profile $\chi(x, t)$ shown in Figure 24a,b depict the complicated and time-dependent transportation behavior of gyrotactic microorganisms in the pulsatile tetra-hybrid nanofluid flow. Contour plot Figure 24a analysis shows that the density of microorganisms is higher in the central core and gradually decreases towards the arterial wall, which eminently reflects an influence due to hydrodynamic shear and motility-modified diffusion near the thin boundary layer. Its temporal variations along the time axis are also found to be significant, indicating that microorganism transfer is highly phase-dependent on the pulsatile nature of the flow; in high-shear parts of the pulse cycle, microorganisms move far away from the wall, while in low-shear ones, partial re-accumulation may be observed. This spatiotemporal phenomenon is also highlighted in the three-dimensional surface plot Figure 24b, depicting a non-uniform decrease in microorganisms vs. radial position combined with slow attenuation in time that results from stronger bioconvective diffusion and interaction with nanoparticle concentration gradients as well as temperature fields.

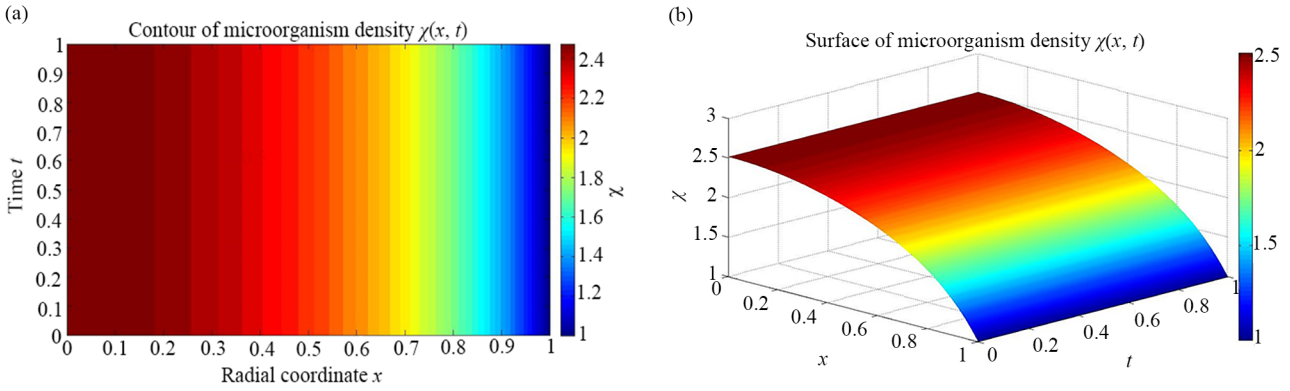


Figure 24. (a) Contour; (b) Surface plot for microoganism profile

5.6 *Entropy generation and Bejan number*

Figure 25a,b show the consequence of entropy generation and its absolute error against distinct *Br*. The entropy generation N_s increases as the Brinkman number *Br* rises, because *Br* measures the ratio of viscous heat dissipation to conductive heat transfer; higher *Br* values indicate that viscous friction—exacerbated by the complex flow caused by stenosis and the presence of nanoparticles—plays a significant role in irreversible behavior, leading to a substantial increase in thermodynamic losses throughout the system. Figure 26a,b show the consequence of Bejan number and its absolute error against distinct *Br*. The Bejan number *Be* decreases as increasing viscous dissipation overcomes the contribution of

thermal conduction and shifts away from heat transfer domination, as observed in the Figure 26a. This points to a crucial trade-off in the diseased artery wall in practical biomedical applications. Figure 27a,b show the consequence of entropy generation and its absolute error also Figure 28a,b show the consequence of Bejan number and its absolute error against distinct ω. The entropy generation N_s increases as the temperature ratio factor ω increases, primarily because a higher ω signifies a larger temperature gradient between the blood/nanofluid and the arterial wall, which leads to greater thermal irreversibility during the heating process along the steeper gradient of the two-sided dilated region, resulting in increased overall thermodynamic losses in the system. Meanwhile, the Bejan number *Be*—being an index that reflects the proportion of entropy generation due to heat transfer irreversibility—also increases as a higher temperature gradient gives dominance to heat transfer irreversibility in comparison with viscous dissipation and other effects, as clearly shown in Figures 27a and 28a, which increase for greater ω.

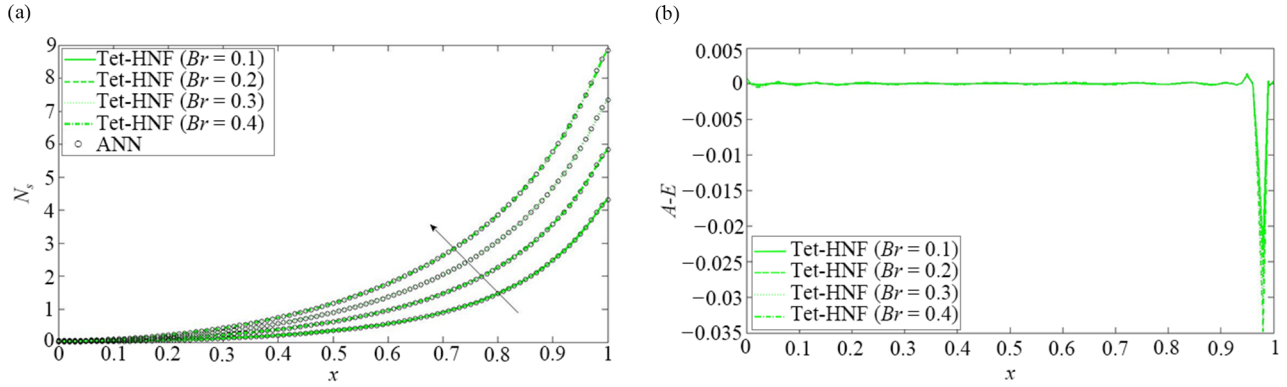


Figure 25. (a) N_s via *Br*; (b) Absolute error

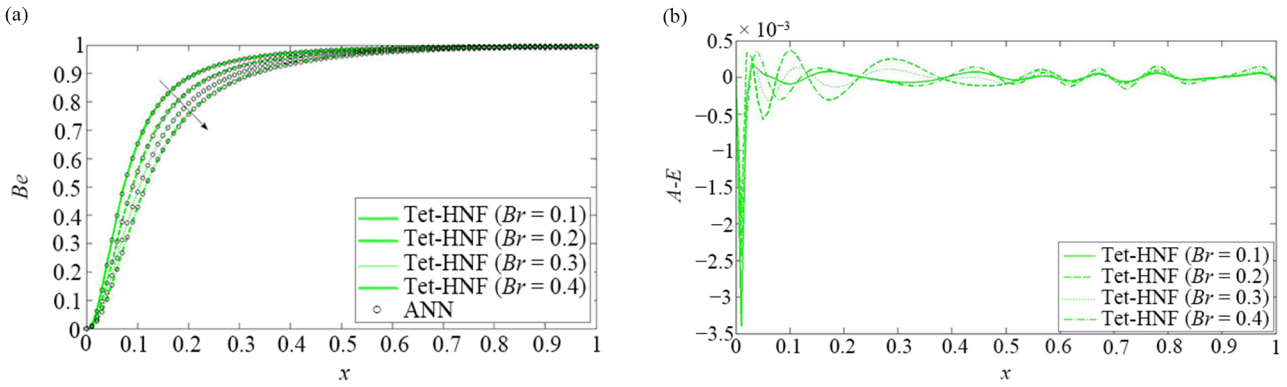


Figure 26. (a) *Be* via *Br*; (b) Absolute error

5.7 *Volume flow rate and wall shear rate*

The volumetric flow rate decreases as the magnetic parameter *M* increases, primarily due to the retarding Lorentz force that opposes the fluid momentum; however, this decrease is less pronounced at high values of the parameter β_0, as indicated by the reduced slope of the flow rate curves in the Figure 29. This is because higher β_0 enhances the effective viscosity and structural rigidity of the Jeffrey nanofluid, which partially counteracts the flattening effect of the applied magnetic field. At the same time, wall shear stress decreases with *M* shown in Figure 30 for the reasons also mentioned above: the wall shear rate diminishes the Lorentz force at small scales, while this trend is again more noticeable at smaller

β_0 since in those cases, the fluid's intrinsic viscosity resistance to flow is weaker and more affected by magnetic damping, causing a larger drop of shear stress.

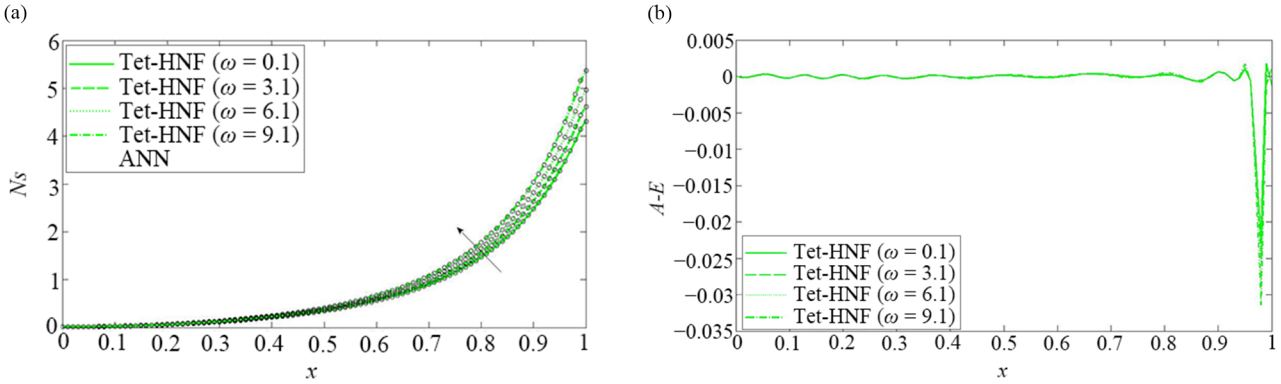


Figure 27. (a) N_s via ω; (b) Absolute error

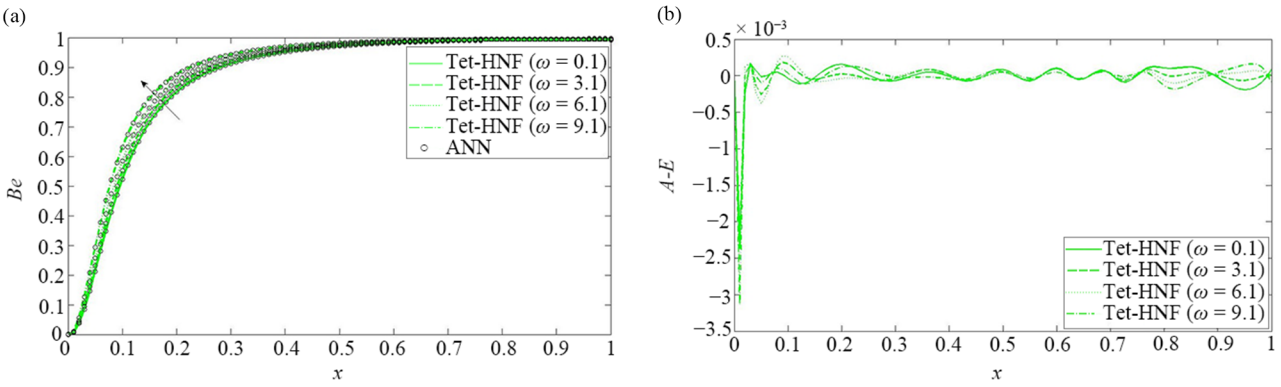


Figure 28. (a) *Be* via ω; (b) Absolute error

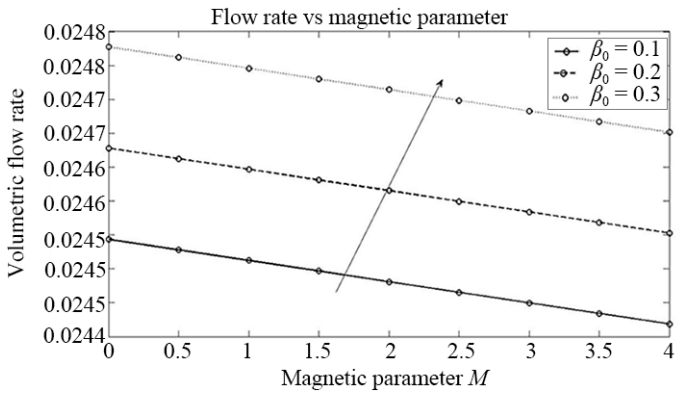


Figure 29. Variation of volumetric flow rate against M for distinct β_0

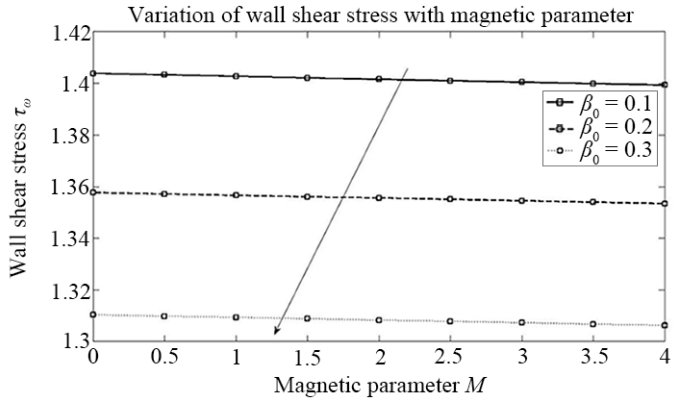


Figure 30. Variation of wall shear stress against M for distinct β_0

6. Conclusions

In the present work, a thorough numerical and data-based analysis is undertaken to investigate mixed convection unsteady flow of tetra-hybrid nanofluid with bioconvective microorganism transport in the presence of a magnetic field combined with unsteady streaming flow at a lower rigid stretching sheet. The nonlinear partial differential equations governing the problem were discretized using a stable implicit FDM utilizing the Thomas algorithm to guarantee stability and accuracy for the highly coupled field variables, i.e., momentum, energy, nanoparticle concentration, and microorganism density. In the course of improving predictive performance, an ANN model was additionally constructed and calibrated based on the numerically simulated data set so that flow and transport characteristics can be predictably evaluated over a broad range of influencing parameters. The comparative analysis indicated that the ANN predictions and numerical solution are in excellent agreement, signifying the efficiency of the proposed hybrid numerical–machine learning framework for simulation of complex MHD nanofluid bioconvective systems. Here's an overview of some of the findings from the above analysis:

• The Jeffrey fluid parameter (λ_1) promotes velocity due to shear thinning and the stretching effect, leading to elastic energy release, whereas the magnetic parameter (M) resists flow due to Lorentz forces but increases temperature by increasing Joule heating. The pulse pressure gradient (B_1) directly enhances velocity; on the other hand, the Eckert number (Ec) and heat generation parameter (Q) distinctly enhance temperature distribution, which illustrates indispensable connections between flow boosting in comparison with thermal resistance.

• Thermophoresis enhances the concentration of particles on cooler surfaces, while Brownian motion promotes diffusion and diminishes peak concentrations. The cell density grows with its buoyancy parameter but decays with the Schmidt number, which suggests that bioconvective control is essential in medical treatments.

• The Br number increases entropy generation by enhancing viscous dissipation, thus reducing the Bejan number (Be), whereas the temperature-difference parameter (ω) reinforces both entropy and Be, leading to irreversibility domination toward heat transfer. This highlights the necessity to balance viscous and thermal loss in order to obtain thermodynamic optimization.

• The ANN surrogate models of the velocity, temperature, concentration, microorganism density, entropy generation, and Bejan number all showed excellent agreements with a negligible MSE (of the order of 10^{-8}–10^{-9}), perfect regression fits $(R = 1)$, and zero-centered error distributions. This supports the ANN as an accurate and efficient substitute for the FDM solver machine learning tool for fast multi-parametric investigation/entropy-based design optimization.

• The findings suggest that external magnetic fields may be manipulated to selectively modulate wall shear stresses and flow rates, which might provide a noninvasive means for stabilizing vulnerable plaque or treating aneurysms. Moreover,

the thermodynamics of entropy generation guides a rational design towards an optimization of nanofluid-mediated drug-delivery systems to minimize hemodynamic and thermal inefficiencies for personalized and physiologically optimized cardiovascular therapies.

In conclusion, to the best of our knowledge, this study is the first successful attempt at amalgamating state-of-the-art fluid dynamics & thermodynamics with machine learning—thus presenting an integrated solution for studying and optimizing complex hemodynamic-thermodynamic processes in diseased arteries, which has direct implications for devising transformative biomedical interventions.

7. Limitation of the study

• The current study utilizes a simplified axisymmetric time-dependent stenotic arterial geometry, which may not represent the complex and patient-specific anatomy observed in various stenosis cases.

• Blood flow is modeled using assumptions of simplicity and effective thermo-physical properties of the tetra-hybrid nanofluid that may not completely reflect the complex characteristics deriving from the rheological and biochemical nature of living blood within in vivo microenvironments.

• Neither arterial wall elasticity, wall deformation, nor complete fluid–structure interaction is explicitly implemented in the current model, and it is likely that these would significantly affect hemodynamic and thermal characteristics within realistic pulsatile flow.

• Also, the ANN model in this study is trained and validated using numerically generated data derived from FDM instead of experimental or clinic datasets; therefore, its predictive performance is currently limited to the computational domain considered in this study.

• This study is mostly theoretical and computational in nature without direct experimental, in vitro, or clinical validation.

Author contributions

All authors participated equally to the conceptualization, investigation, analysis, original draught Writing, review, and editing of the work.

Acknowledgement

Authors Nahid Fatima and Kamaleldin Abodayeh are thankful to Prince Sultan University for APC and support through TAS research lab.

Data availability statement

The data that support the findings of the study are available from the corresponding author upon reasonable request.

Conflict of interest

The authors declare no competing financial interest.

References

[1] Young DF. Effect of a time-dependent stenosis on flow through a tube. *Journal of Engineering for Industry*. 1968; 90(2): 248–254. Available from: https://doi.org/10.1115/1.3604621.

[2] MacDonald DA. On steady flow through modelled vascular stenoses. *Journal of Biomechanics*. 1979; 12(1): 13–20. Available from: https://doi.org/10.1016/0021-9290(79)90004-6.

[3] Shareghi S, Toghraie D. Numerical simulation of blood flow in healthy arteries by use of the Sisko model. *Computational Thermal Sciences: An International Journal*. 2016; 8(4): 309–320. Available from: https://doi.org/10.1615/ComputThermalScien.2016016738.

[4] Shahzadi I, Bilal S. A significant role of permeability on blood flow for hybrid nanofluid through bifurcated stenosed artery: drug delivery application. *Computer Methods and Programs in Biomedicine*. 2020; 187: 105248. Available from: https://doi.org/10.1016/J.CMPB.2019.105248.

[5] Singh S, Nandkeolyar R. Modeling blood flow with tetra-hybrid Casson nanofluid in stenosed arteries: numerical and machine learning approach. *Journal of Thermal Stresses*. 2026; 49(4): 570–598. Available from: https://doi.org/10.1080/01495739.2025.2578599.

[6] Sudarmozhi K, Devi VS, Öztop HF, Ahmad H, Abd-Elmonem A, Jamshed W, et al. AI-neural network modelling of Williamson blood flow in porous medium Soret-Dufour effects with tetra hybrid nanoparticles. *International Communications in Heat and Mass Transfer*. 2026; 171: 110107. Available from: https://doi.org/10.1016/j.icheatmasstransfer.2025.110107.

[7] Singh A, Nazir U, Ahmed MA, Al-Mekhlafi SM, AL Garalleh H, Galal AM. Computational study of tetra hybrid nanofluid in micropolar fluid on shrinking/stretching needle: a dual solution study. *International Journal of Thermofluids*. 2026; 32(37): 101576. Available from: https://doi.org/10.1016/j.ijft.2026.101576.

[8] Hafed ZS, Arafa AAM, Hussein SA, Ahmed SE, Morsy Z. Bioconvective blood flow of tetra composition nanofluids passing through a stenotic artery with Arrhenius energy. *Numerical Heat Transfer, Part B: Fundamentals*. 2025; 86(3): 580–603. Available from: https://doi.org/10.1080/10407790.2023.2289505.

[9] Alghamdi W, Alsubie A, Kumam P, Saeed A, Gul T. MHD hybrid nanofluid flow comprising the medication through a blood artery. *Scientific Reports*. 2021; 11(1): 11621. Available from: https://doi.org/10.1038/s41598-021-91183-6.

[10] Saeed A, Alsubie A, Kumam P, Nasir S, Gul T, Kumam W. Blood based hybrid nanofluid flow together with electromagnetic field and couple stresses. *Scientific Reports*. 2021; 11(1): 12865. Available from: https://doi.org/10.1038/s41598-021-92186-z.

[11] Nadeem S, Ijaz S, Sadiq MA. Inspiration of induced magnetic field on a blood flow of Prandtl nanofluid model with stenosis. *Current Nanoscience*. 2014; 10(5): 753–765. Available from: https://doi.org/10.2174/15734137106661406120103333.

[12] Majee S, Shit GC. Numerical investigation of MHD flow of blood and heat transfer in a stenosed arterial segment. *Journal of Magnetism and Magnetic Materials*. 2017; 424: 137–147. Available from: https://doi.org/10.1016/J.JMMM.2016.10.028.

[13] Sharma BK, Gandhi R, Bhatti MM. Entropy analysis of thermally radiating MHD slip flow of hybrid nanoparticles (Au-Al_2O_3/Blood) through a tapered multi-stenosed artery. *Chemical Physics Letters*. 2022; 790: 139348. Available from: https://doi.org/10.1016/J.CPLETT.2022.139348.

[14] Gandhi R, Sharma BK, Makinde OD. Entropy analysis for MHD blood flow of hybrid nanoparticles (Au–Al_2O_3/blood) of different shapes through an irregular stenosed permeable walled artery under periodic body acceleration: hemodynamical applications. *ZAMM - Journal of Applied Mathematics and Mechanics*. 2022; 106(2): e202100532. Available from: https://doi.org/10.1002/ZAMM.202100532.

[15] Sharma BK, Kumawat C, Bhatti MM. Optimizing energy generation in power-law nanofluid flow through curved arteries with gold nanoparticles. *Numerical Heat Transfer, Part A: Applications*. 2024; 85(18): 3058–3090. Available from: https://doi.org/10.1080/10407782.2023.2232123.

[16] Sharma BK, Gandhi R. Entropy-driven optimization of radiative Jeffrey tetrahybrid nanofluid flow through a stenosed bifurcated artery with Hall effects. *Physics of Fluids*. 2023; 35(12). Available from: https://doi.org/10.1063/5.0179798.

[17] Nadeem S, Ijaz S, Akbar NS. Nano particle analysis for the steady blood flow of Jeffrey fluid with stenosis with new analytical techniques. *Journal of Computational and Theoretical Nanoscience*. 2013; 10(11): 2751–2765.

[18] Padma R, Tamil Selvi R, Ponalagusamy R. Effects of slip and magnetic field on the pulsatile flow of a Jeffrey fluid with magnetic nanoparticles in a stenosed artery. *European Physical Journal Plus*. 2019; 134(5): 221. Available from: https://doi.org/10.1140/EPJP/I2019-12538-9.

[19] Kumar A, Sharma BK, Gandhi R, Mishra NK, Bhatti MM. Response surface optimization for the electromagnetohydrodynamic Cu-polyvinyl alcohol/water Jeffrey nanofluid flow with an exponential heat source.

Journal of Magnetism and Magnetic Materials. 2023; 576: 170751. Available from: https://doi.org/10.1016/J.JMMM.2023.170751.

[20] Ali A, Barman A, Das S. Electromagnetic phenomena in cilia actuated peristaltic transport of hybrid nano-blood with Jeffrey model through an artery sustaining regnant magnetic field. *Waves in Random and Complex Media*. 2025; 35(3): 5710–5741. Available from: https://doi.org/10.1080/17455030.2022.2072533.

[21] Çolak AB, Shafiq A, Sindhu TN. Modeling of Darcy–Forchheimer bioconvective Powell Eyring nanofluid with artificial neural network. *Chinese Journal of Physics*. 2022; 77: 2435–2453. Available from: https://doi.org/10.1016/J.CJPH.2022.04.004.

[22] Shafiq A, Çolak AB, Sindhu TN. Comparative analysis to study the Darcy-Forchheimer Tangent hyperbolic flow towards cylindrical surface using artificial neural network: an application to parabolic trough solar collector. *Mathematics and Computers in Simulation*. 2024; 216: 213–230. Available from: https://doi.org/10.1016/J.MATCOM.2023.09.014.

[23] Qureshi MZA, Faisal M, Malik KR, Shah NA. Computing of temperature-dependent thermal conductivity and viscosity correlation for solar energy and turbulence appliances via artificial neural network algorithm. *Modern Physics Letters B*. 2024; 38(14). Available from: https://doi.org/10.1142/S0217984924501045.

[24] Ermis K, Erek A, Dincer I. Heat transfer analysis of phase change process in a finned-tube thermal energy storage system using artificial neural network. *International Journal of Heat and Mass Transfer*. 2007; 50(15–16): 3163–3175. Available from: https://doi.org/10.1016/J.IJHEATMASSTRANSFER.2006.12.017.

[25] Shah Z, Asif M, Sulaiman M, Antonescu E. A novel hybrid computational-neural framework to the mechanisms of blood flow and thermal transport in non-planar curved arteries. *Case Studies in Thermal Engineering*. 2006; 83: 108200. Available from: https://doi.org/10.1016/j.csite.2026.108200.

[26] Ur Rehman K, Shatanawi W, Yian LY. Artificial intelligence based analysis for magnetized Casson fluid in partially heated cavity rooted with heated fin. *International Journal of Thermofluids*. 2025; 26: 101095. Available from: https://doi.org/10.1016/J.IJFT.2025.101095.

[27] Kousar N, Rehman KU, Fatima N, Shatanawi W, Asghar Z. Neural networking analysis on heat transfer in Casson fluid with mixed convection equipped in staggered cavity with anti-parallel moving boundary. *International Journal of Thermofluids*. 2025; 26: 101053. Available from: https://doi.org/10.1016/J.IJFT.2025.101053.

[28] Rehman KU, Shatanawi W, Asghar Z, Kasim ARM. Neural networking analysis of thermally magnetized mass transfer coefficient (MTC) for Carreau fluid flow: a comparative study. *International Journal of Thermofluids*. 2025; 26: 101069. Available from: https://doi.org/10.1016/J.IJFT.2025.101069.

[29] Ahmed A, Nadeem S. Effects of magnetohydrodynamics and hybrid nanoparticles on a micropolar fluid with 6-types of stenosis. *Results in Physics*. 2017; 7: 4130–4139. Available from: https://doi.org/10.1016/J.RINP.2017.10.032.

[30] Tripathi J, Vasu B, Bég OA, Mounika BR, Gorla RSR. Numerical simulation of the transport of nanoparticles as drug carriers in hydromagnetic blood flow through a diseased artery with vessel wall permeability and rheological effects. *Microvascular Research*. 2022; 139: 104241. Available from: https://doi.org/10.1016/J.MVR.2021.104241.

[31] Zaman A, Sajid M, Kousar N. Biomedical study of effects nanoparticles on unsteady blood (non-Newtonian) flow through a catheterized stenotic vessel. *Canadian Journal of Physics*. 2019; 97(5): 487–497. Available from: https://doi.org/10.1139/CJP-2018-0376.

[32] Gandhi R, Sharma BK, Al-Mdallal QM, Mittal HVR. Entropy generation and shape effects analysis of hybrid nanoparticles (Cu-Al2O3/blood) mediated blood flow through a time-variant multi-stenotic artery. *International Journal of Thermofluids*. 2023; 18: 100336. Available from: https://doi.org/10.1016/J.IJFT.2023.100336.

[33] Zaman T, Shah Z, Rooman M, Khan W, Alshehri MH, Vrinceanu N. Rheological analysis of magnetized trihybrid nanofluid drug carriers in unsteady blood flow through a single-stenotic artery. *Chinese Journal of Physics*. 2024; 91: 538–559. Available from: https://doi.org/10.1016/J.CJPH.2024.08.002.

[34] Sharma BK, Khanduri U, Gandhi R, Muhammad T. Entropy generation analysis of a ternary hybrid nanofluid (Au-CuO-GO/blood) containing gyrotactic microorganisms in bifurcated artery. *International Journal of Numerical Methods for Heat and Fluid Flow*. 2024; 34(2): 980–1020. Available from: https://doi.org/10.1108/HFF-07-2023-0439.

[35] Tripathi J, Vasu B, Bég OA, Gorla RSR. Unsteady hybrid nanoparticle-mediated magneto-hemodynamics and heat transfer through an overlapped stenotic artery: biomedical drug delivery simulation. *Proceedings of the Institution of Mechanical Engineers, Part H: Journal of Engineering in Medicine*. 2021; 235(10): 1175–1196. Available from: https://doi.org/10.1177/09544119211026095.